HHS Public Access

Author manuscript

Neuron. Author manuscript; available in PMC 2025 January 03.

Published in final edited form as:

Neuron. 2024 January 03; 112(1): 141–154.e8. doi:10.1016/j.neuron.2023.10.002.

Dopamine pathways mediating affective state transitions after sleep loss

Mingzheng Wu[1,2], **Xin Zhang**[1], **Sihan Feng**[1], **Sara N. Freda**[1], **Pushpa Kumari**[1], **Vasin Dumrongprechachan**[1,3], **Yevgenia Kozorovitskiy**[1,3,4]

[1]Department of Neurobiology, Northwestern University, Evanston, IL 60208, USA

[2]Querrey Simpson Institute for Bioelectronics, Northwestern University, Evanston, IL 60208, USA

[3]Chemistry of Life Processes Institute, Northwestern University, Evanston, IL 60208, USA

[4]Lead Contact

SUMMARY

Pathophysiology of affective disorders—particularly circuit-level mechanisms underlying bidirectional, periodic affective state transitions—remains poorly understood. In patients, disruptions of sleep and circadian rhythm can trigger transitions to manic episodes, while depressive states are reversed. Here, we introduce a hybrid automated sleep deprivation platform to induce transitions of affective states in mice. Acute sleep loss causes mixed behavioral states featuring hyperactivity, elevated social and sexual behaviors, and diminished depressive-like behaviors, where transitions depend on dopamine. Using dopamine sensor photometry and projection-targeted chemogenetics, we reveal that elevated dopamine release in specific brain regions mediates distinct behavioral changes in affective state transitions. Acute sleep loss induces dopamine-dependent enhancement in dendritic spine density and uncaging-evoked dendritic spinogenesis in the medial prefrontal cortex, whereas optically mediated disassembly of enhanced plasticity reverses the antidepressant effects of sleep deprivation on learned helplessness. These findings demonstrate that brain-wide dopaminergic pathways control sleep loss-induced polymodal affective state transitions.

eTOC Blurb:

Sleep perturbations are known to alter mood. Wu et al. show that specific dopaminergic pathways regulate distinct behavioral changes induced by brief sleep deprivation. Optically

Corresponding author: Yevgenia.Kozorovitskiy@northwestern.edu.

AUTHOR CONTRIBUTIONS

Conceptualization, M.W. and Y.K.; Methodology, M.W. and Y.K.; Formal Analysis, M.W., X.Z. and S.N.F.; Data Curation, M.W., X.Z., S.F.; Investigation, M.W., X.Z., S.F, S.N.F., P.K., V.D.; Writing – Original Draft, M.W. and Y.K.; Writing – Review & Editing, M.W., X.Z., S.F, S.N.F., P.K., V.D. and Y.K.; Funding Acquisition, Y.K.; Supervision, Y.K.

DECLARATION OF INTERESTS

The authors declare no competing interests.

mediated disassembly of enhanced neuroplasticity revealed a dopamine-dependent mechanism that maintains the antidepressant effects of acute sleep loss.

INTRODUCTION

Affective disorders, characterized by significant mood disturbances, are prevalent and recurrent psychiatric disorders that diminish quality of life and increase mortality[1,2]. Predominant affective disorder states are depression, featuring sadness and loss of interest in activities, and mania, characterized by elevated mood and overactivity that impair cognitive function[3-6]. Transitions among affective states occur episodically. Environmental, behavioral, and pharmacological perturbations can evoke affective state transitions in healthy subjects[7-10] and in mood disorder patients[11-13]. The neural mechanisms underlying episodical changes in affect may be exacerbated by pathological alterations at genetic, cellular, and neural circuit levels[14-18], leading to lasting psychiatric mood episodes in affective disorders[11,19-21]. However, the mechanisms initiating affective state transitions remain poorly understood. Elucidating the neuromodulatory pathways underlying physiological changes in affective states is important for understanding mechanisms that are involved in the pathogenesis of affective disorders and developing new treatment approaches.

Alterations in sleep and circadian rhythms are common features in affective disorders[20,22-24]. Moreover, manipulations of sleep and circadian rhythms often drive changes in affective states in animal models[25]. The disruption of circadian rhythm and sleep can reproduce a cluster of behavioral features of mania, triggering manic episodes in patients with bipolar disorder[12,26,27]. Sleep deprivation and chronobiological treatments can reverse depressive episodes[28], suggesting that sleep loss induces a global switch of affective states. Affective state changes induced by sleep deprivation have been validated in multiple species[29-33]. Therefore, sleep deprivation is an experience-driven experimental paradigm that can facilitate identification of underlying neuromodulatory mechanisms in affective state transitions, without relying on global genetic perturbations or pharmacological treatments that broadly alter neural circuit function.

Changes in the dopaminergic system have been broadly implicated in affective disorders and sleep regulation[34-40]. Dynamics of dopaminergic neuronal activity and release regulate sleep stages[41,42]. Manipulations of circadian regulatory genes alter dopaminergic activity in distributed brain circuits[14,43,44], generating depressive, manic-like, or mixed behavioral states[15,19,45,46]. Here, we describe a framework where dopaminergic pathways mediate affective state transitions physiologically induced by acute sleep loss in mice without genetic or pharmacological perturbations associated with bipolar disorder in humans. Using behavioral, genetically targeted, and projection-specific chemogenetic manipulations, we dissected the functions of distinct subgroups of DA neurons in state transitions characterized by elevated activity across several behavioral domains and diminished depressive-like behavior. Optically mediated disassembly of enhanced plasticity associated with affective state transitions revealed a dopamine-dependent plasticity mechanism that maintains the antidepressant effects of acute sleep loss.

RESULTS

Acute sleep deprivation induces affective state transitions

We developed a hybrid sleep deprivation (SD) paradigm combining elements of the traditional flowerpot[29] and the rotating beam[47] methods to automatically disrupt sleep in mice without imposing requirements for continual motion (Figure 1A). The device is a cylindrical chamber with a small, elevated platform (3 cm diameter) above a slowly rotating beam that covers the floor area. Animals choose between resting on the small, elevated platform or maintaining locomotion to negotiate the slowly rotating beam. While retaining the benefits of automation, this hybrid SD method eliminates the risk of water immersion in the 'flowerpot' method and forced locomotor activity in the 'propeller' method. We validated the effectiveness of this hybrid SD method using EEG/EMG recordings, showing that NREM and REM sleep were significantly reduced in the SD device compared to home cage controls (Figure 1A, Figure S1A-C).

We used this new hybrid SD method to induce behavioral state transitions featuring hyperactivity, aggression, and hypersexuality[32]. Specific behavioral domains were assessed after separate SD sessions (Figure S2A). Mice showed elevated locomotor activity after twelve-hour acute SD compared to baseline, while the control group remaining in their home cages did not display locomotion changes (Figure 1B-D). Next, we tested the behavioral effects of acute SD on a spectrum of social behaviors in sexually experienced male mice living in dyads with oviductectomized females (Figure 1E). In the baseline, a small proportion of mice (7/25) displayed aggressive behavior towards a smaller intruder in the resident-intruder paradigm. After SD, the proportion of mice expressing aggressive behavior increased (22/25), leading to a change in the overall distribution of durations for aggressive actions (Figure 1F, G). The time spent engaging in social interactions and aggressive behaviors towards male intruders was significantly elevated after SD (Figure 1H). We separated the resident mice into aggressors and non-aggressors based on time spent attacking intruders. Resident mice that displayed aggressive behavior in the baseline (aggressors) did not show significant increases in social interactions and aggression after SD, consistent with a possible behavioral or physiological ceiling effect (Figure S2B-E). Thus, for subsequent experiments measuring social and aggressive behavior (Figures 2-4), we restricted the analyses to the majority of mice that did not display aggression in the baseline, since their behavioral state changes could be robustly identified.

Furthermore, we observed increased sexual behavior towards receptive females in the resident mice after acute SD. A higher proportion of mice (83%, 20/23) displayed sexual behaviors (mounting and intromission) towards receptive females after SD, compared to 61% (14/23) in the baseline (Figure 1I-K). Time spent engaging in sexual behavior was significantly increased after SD, while the total social interaction time in male-female pairs was not altered (Figure 1L). These findings demonstrate that several ethologically relevant behavioral categories are altered in the hybrid acute SD paradigm, confirming the transition to a distinct affective state relative to baseline.

To define the effects of acute sleep loss on affective transitions in depressive-like states, we tested the effects of acute SD on stress-induced aversive learning and anhedonia using

a learned helplessness (LH) model in animals with prior experience of acute SD-induced behavioral changes. Our previous work showed that LH induction (360 inescapable foot zaps per day for two sequential days) elicits a distinctive depressive-like state, quantified by decreased escape actions for an avoidable unpleasant stimulus[48-50] (Figure 1M). This form of aversive learning was rapidly and persistently reversed by acute 12-hour-long SD, evidenced by a substantial reduction in escape failures, measured 30 min and 24 hrs after the SD period ended (Figure 1N). Controls remaining in their home cages did not show changes in escape behavior after LH, demonstrating that the observed effects were not caused by time-dependent learning extinction[50] (Figure 1N). We carried out the sucrose preference tests for 12 hrs in the homecage after the completion of LH testing. Mice showed decreased preference for 1% sucrose solution after LH induction, and diminished sucrose preference was reversed after acute SD (Figure 1O).

For a subset of animals, we tracked behavioral changes across subsequent days after the acute SD period. Elevated locomotion and sexual behavior no longer significantly differed from baseline 24 hrs after SD (Figure S3). Time spent engaged in social interactions and aggression towards male intruders returned to baseline levels 48 hrs after SD. Yet, the reversal of learned helplessness behavior, measured as a reduction in escape failures, lasted at least 72 hrs after a single acute SD period, although preference for the sucrose solution was no longer significantly different from the LH condition 24 hrs after SD. These results suggest that affective state transitions are relatively transient in subjects without pathological backgrounds. Correlative analyses revealed a positive correlation between elevated aggression and social behavior after SD ($R^2 = 0.67$, $p = 0.0069$), and a negative correlation between increased sexual behavior and reduction of escape failures ($R^2 = 0.74$, $p = 0.0028$). No significant correlations were found among other pairs of behavioral categories. Finally, we performed additional control experiments using devices with larger platforms (6 cm diameter) that allow animals to sleep (Figure S4A). None of the behavioral changes after acute SD were observed using large platform devices, suggesting that environmental cues alone are insufficient for behavioral transitions (Figure S4B-G). In sum, acute SD evoked the transition to a hyperactive state but normalized a depressive-like state, raising the question of whether these two directions of state transitions depend on the same or different neural mechanisms.

Affective state transitions induced by acute SD are dopamine-dependent

Given the substantial work linking dopamine to human affective disorders and related behavioral features in rodent models, we next tested whether DA activity is necessary for SD-induced behavioral state transitions. We confirmed that DA neuronal activity was elevated during SD using fiber photometry of GCaMP6f-expressing DA neurons in the ventral tegmental area (VTA). Using a template-matching method, we detected increased amplitude of spontaneous calcium transients in VTA DA neurons during SD, compared to home cage controls during the light phase (ZT6) (Figure 2A-C, Figure S5A-C).

We then used the inhibitory DREADD hM4Di to suppress the activity of VTA DA neurons[50,51]. DAT^{iCre} positive neonates and their Cre-negative littermates were virally transduced with AAV1.CBA.DIO.hM4Di.mCherry (Figure 2D). Expression of hM4Di was

confined within the VTA (Figure 2D), and DREADD-dependent inhibition of spontaneous neuronal activity in VTA DA neurons was validated using cell-attached recording in the acute slice (Figure 2E). We injected three doses of CNO (1 mg/kg, i.p.) every 4 hrs starting from the onset of SD (ZT0) in $hM4Di^+$ animals and Cre-negative littermate controls ($hM4Di^-$). While chemogenetic inhibition of VTA DA neurons has been shown to promote sleep[41], the hybrid SD paradigm sufficed to suppress sleep in the background of reduced VTA DA neuron activity (Figure S5D, E). SD-associated hyperactivity was blocked by CNO treatment in $hM4Di^+$ animals, but not in CNO-treated $hM4Di^-$ controls (Figure 2F). Inhibition of VTA DA neurons in the absence of SD did not reduce locomotor activity. In male-male social interaction tests, acute SD no longer altered social interaction length or aggression after chemogenetic inhibition of VTA DA activity during SD (Figure 2G). However, inhibition of VTA DA neurons did not abolish the SD-induced increase in sexual behavior, suggesting that hypersexuality after SD may depend on a different group of DA neurons or on other neural circuits (Figure 2H). Finally, we tested whether the SD-induced transition from a depressive-like state requires DA. Inhibition of VTA DA neuron activity during SD blocked the reversal of escape behaviors after LH, confirming that SD-induced state transitions in LH are DA-dependent (Figure 2I). The increase in sucrose preference after acute SD was likewise abolished (Figure 2I). These data implicate DA-dependent dynamics as underlying mechanisms for polymodal affective state transitions evoked by acute SD in mice without BD-associated pathological background.

Sleep perturbation amplifies spontaneous DA release in distributed brain regions

Emerging evidence supports a framework where DA regulates behaviors by modulating neuronal activity in specific, task-relevant DA-recipient regions[52]. Transitions in affective states span changes across distinct behavioral domains that are likely regulated by DA through multiple downstream brain networks. We measured dopamine release in several DA-recipient regions during the SD period using a genetically encoded GPCR activation-based DA sensor ($GRAB_{DA}$)[53]. We separately monitored DA release with fiber photometry in the nucleus accumbens (NAc), medial prefrontal cortex (mPFC), hypothalamic area (HA), and dorsal striatum (dStr). DAT^{icre} mice with $GRAB_{DA}$ expression in relevant DA-recipient regions were virally transduced with hM4Di in the corresponding dopaminergic neuronal populations: VTA DA neurons for NAc and mPFC, hypothalamic DA neurons for HA, and SNc DA neurons for dStr. We compared spontaneous DA release in the home cage and during SD in the light phase (ZT6). In the NAc, we observed two types of DA transients with different kinetics. Slow, lasting DA ramps (~100-sec duration) were amplified during SD, resulting in increased DA release measured by area under the curve (AUC) in spontaneous transients (Figure 3A-C). In addition, rapid DA transients (~5-sec duration) were also significantly increased in AUC during SD (Figure S6A). Chemogenetic inhibition of VTA DA neurons significantly suppressed DA levels, evident in the reduction of AUC for slow $GRAB_{DA}$ transients (Figure 3C). In the mPFC and HA (Figure 3D, G), DA ramps were predominant, accounting for most spontaneous DA release events (Figure 3E, H, Figure S6B, C). Spontaneous $GRAB_{DA}$ transients in the mPFC and HA were amplified during SD, enhancing cumulative transient-associated DA release in the AUC. In addition, the frequency of DA transients in mPFC and HA during SD was significantly higher than in the home cage (Figure S6B, C). Chemogenetic inhibition of the corresponding groups of

DA neurons suppressed the AUC changes for DA transients in both mPFC and HA (Figure 3F, I). In contrast, low-frequency DA ramps, the more prevalent high-frequency short DA transients, and the AUC associated with them in the dStr remained unchanged during SD (Figure 3J-L, Figure S6D). These findings confirm that sleep perturbation amplifies spontaneous DA release across a broad network of regions implicated in regulating affective behavior. Fiber placements for all animals were confirmed histologically and aligned to the Common Coordinate Framework (Figure S7)[54].

Distinct modulation of state transitions by dopaminergic pathways

We used projection-specific chemogenetic inhibition of DA neurons to dissect the dopaminergic regulation of behavioral changes in affective state transitions induced by acute sleep loss. To achieve projection-specific control, we combined the Th-2A-Flpo mouse line[55] to restrict viral expression to Th^+ dopaminergic neurons and a retrograde adeno-associated virus (rgAAV) that infects axons in the target site. We injected rgAAV.EF1α.fDIO.Cre virus into several regions containing DA terminals in Th-2A-Flpo mice and subsequently injected them with AAV1.CBA.DIO.hM4Di.mCherry to transduce DA neuron cell bodies. Using this dual-virus strategy, we transduced hM4Di in DA neurons whose primary targets were, respectively, the nucleus accumbens (NAc), medial prefrontal cortex (mPFC), hypothalamic regions, and dStr (Figure 4A). Subgroups of DA neurons showed distinct primary projection patterns and collateral targets, with some projection overlap from injections seeded in different sites, as demonstrated in previous studies[55-58]. For example, in our dataset, the highest amount of axonal labeling for VTA DA neurons retrogradely transduced with rAAV injections in the NAc and mPFC was in the NAc vs mPFC (IL), respectively. The highest labeling density for hypothalamic DA neurons was observed in the medial preoptic nucleus (MePN) and the broader medial preoptic area (mPOA) (Figure S8).

Next, we assessed the engagement of these DA neuron subgroups in state transitions induced by acute SD. During the SD period, the activity of target subgroups was inhibited by CNO administration (1 mg/kg every 4 hrs, i.p., Figure 4B). We first sought to address the role of DA neuron subgroups in SD-induced hyperactivity. It was abolished by inhibiting NAc-projecting DA cells, but not the DA neurons that project to mPFC or hypothalamic regions (Figure 4C). Surprisingly, chemogenetic inhibition of dStr-projecting SNc DA neurons during SD did not abolish the increase in open-filed locomotion. This observation raises the possibility that, despite ample evidence for broad DA signaling involvement in manic-like behavioral changes, hyperactivity after sleep loss may be more related to affective state changes, rather than a dStr-mediated enhancement in voluntary movement. In the resident intruder tests, the inhibition of either mPFC-projecting or hypothalamic DA neurons strongly suppressed the increase in social behaviors after SD, while the inhibition of NAc-projecting DA neurons showed weaker effects on social behaviors (Figure 4D). This lack of pathway-selective effects on social behaviors suggests that elevated sociality may be mediated by diverse DA neuron subgroups projecting, at the minimum, to the NAc, mPFC, and HA. Inhibiting dStr-projecting SNc DA neurons failed to block enhanced social behavior after SD. Aggressive behavior toward male intruders after SD was entirely abolished by inhibiting mPFC-projecting DA neurons, but not DA projections to NAc, HA,

or dStr (Figure 4D). Enhanced sexual behavior towards receptive females was specifically blocked by suppressing the activity of hypothalamic DA neurons, while the inhibition of NAc, mPFC, or dStr projecting DA neurons had no effect (Figure 4E). Finally, to test whether a specific group of DA neurons mediates SD-dependent transition from a depressive-like behavioral state, we tested escape behavior after LH, following acute SD with chemogenetic inhibition of different DA subgroups. The reversal of LH behavior was blocked only when mPFC-projecting DA neurons were inhibited during SD, but not the NAc-projecting, hypothalamus targeting, or dStr-projecting populations (Figure 4F). Altogether, these findings suggest that multiple subgroups of distributed DA projections broadly control the transition to manic-like states, while mPFC-targeting DA neurons more specifically mediate the transition from a depressive-like state.

Acute SD recovers LH resilience through DA-dependent cortical dendritic spinogenesis

Enhanced neuroplasticity in mPFC likely mediates the transition from depressive-like states, as evidenced by the mechanisms underlying the effects of rapidly-acting antidepressants like ketamine and psilocybin[49,59,60]. We have previously demonstrated that ketamine enhanced glutamate-evoked spinogenesis through mechanisms that involve enhancement of dopaminergic tone[49]. Thus, we sought to test whether dendritic spine plasticity in mPFC is similarly enhanced in acute SD-induced behavioral state transitions. Using 2-photon laser scanning microscopy, we compared dendritic spine density on deep-layer mPFC pyramidal neurons for mice in the baseline condition and after acute SD in Thy1-EGFP mice (Figure 5A). Our results showed that dendritic spine density on apical dendrites of deep layer pyramidal neurons in mPFC was significantly increased 24 hrs after SD (Figure 5B). Conditional knock-out of Drd1 in virally transduced GFP-expressing mPFC pyramidal neurons using a dual viral strategy abolished these dendritic spine density changes, demonstrating that acute SD effects on structural plasticity are DA-dependent (Figure 5C). Furthermore, using 2-photon glutamate uncaging to evoke *de novo* spinogenesis (Figure 5D, E), we found that the probability of glutamate-evoked spinogenesis on apical dendrites of deep layer mPFC neurons expressing GFP was increased after acute SD, an effect that was blocked by sparse, virally mediated Drd1 conditional knock-out (Figure 5F). These findings show that acute SD enhances structural synaptic plasticity in mPFC in a DA-dependent manner, similar to the plasticity-driving effects recently described for several rapidly-acting antidepressants[49,60-63].

Next, to directly test whether behavioral state transitions induced by SD require new dendritic spine formation, we used genetically encoded photoactivatable Rac1 (PaRac1) to selectively eliminate recently activated synapses, as previously described[63,64] (Figure 5G). Based on this work, we generated constructs that encode PSD95(Δ1.2)-mVenus-PaRac1 in an activity-dependent manner. Due to the overlap of mVenus spectrum with other fluorophores, we also generated a construct using mScarlet to visualize the expression of PaRac1 with EGFP (Figure S9). We validated the localized expression of PaRac1-mScarlet in dendritic spines of cultured neurons and pyramidal cells in mPFC (Figure S9A-B). Then, using a Rac1 pull-down IP assay[64], we confirmed that altering neural activity with forskolin or light activation enhanced the expression of the activated form of Rac1 in primary cultured neurons (Figure S9C-D). The increase in Rac1 expression by forskolin is downstream of

overall enhancement of cAMP-dependent protein synthesis[65], and the PaRac1 construct is activity-dependent[64], with forskolin providing a positive control for light activation of PaRac1 (Figure S9E). We virally transduced PaRac1 AAV bilaterally into the mPFC, and subsequently implanted a bilateral fiber for photoactivation (Figure 5H). Expression of PaRac1 and fiber location were validated by histology (Figure 5I). To address whether mood state lability after SD requires neuroplasticity, we induced LH in animals expressing PaRac1 and photo-activated PaRac1 (1 h, 470 nm) 30 min or 24 hrs after acute SD. Escape actions were assessed 1 hr after the end of photo-activation (Figure 5J). The activation of PaRac1 30 min after SD did not stop the immediate reversal of LH behaviors, although escape actions were slightly reduced 24 hrs after acute SD followed by PaRac1 activation (Figure 5K). In contrast, the activation of PaRac1 24 hrs after SD strongly reversed the affective state switch induced by acute SD, suggesting that the production or strengthening of neuronal connections in mPFC is essential for maintaining the antidepressant effects of brief sleep loss (Figure 5K). The initiation of this experience-driven state transition from a depressive-like state is linked to the restructuring of dopamine release in mPFC, and its maintenance requires enhanced local neuroplasticity.

DISCUSSION

Here, we create a hybrid method for automated sleep deprivation to evaluate dopaminergic correlates of behavioral state transitions featuring changes across several behavioral domains. This relatively mild and acute sleep perturbation provides a tool to understand and control the affective state lability. We characterize the heterogeneous involvement of distributed dopaminergic networks in SD-associated behavioral changes, where specific projections targeting distinct downstream regions show preferential engagement in different aspects of behavior, from locomotion increases to hypersexuality. In addition, sleep loss evokes a rapid reversal of the depressive-like behaviors specifically regulated by the dopaminergic activity in the mPFC, where the dopamine-dependent enhancement of dendritic plasticity maintains the new affective state. In this study, we focused on mechanisms underlying affective state transitions in animals with no pathological background, revealing important functions of dopaminergic signaling likely relevant in mental health conditions that are challenging to fully model in mice.

DA neurons regulate many ethologically important behaviors, including reinforcement, aversion, social reward, and consummatory responses[50,52,57,66-68], linked to the diverse connectivity profiles of molecularly distinct DA neuron subgroups[55,56,69-72]. We have defined the functional roles of four projection-specific dopaminergic pathways in affective state transitions induced by acute sleep loss. The emergence of hyperactive behavioral phenotypes differentially engages one or more pathways, while transitions from depressive-like states exclusively depend on DA in the mPFC. Our findings suggest that behavioral correlates of DA neuron activity are highly context-dependent. For example, while dStr DA signaling is well-established to be critical for locomotor behavior[73,74], we find that chemogenetic inhibition of dStr-projecting DA neurons does not block locomotor hyperactivity after SD. Thus, the involvement of a DA neuron subgroup in specific behavioral domains may vary across distinct behavioral states, which are shaped by prior experiences (*e.g.,* sleep deprivation) that differentially regulate DA release in projection-

specific manner. Genetic diversity of DA neurons is well-aligned with both projection specificity and functional responses, as shown in a recent study[75]. This likely contributes to the heterogeneity of behavioral phenotypes in affective disorders and varied response to treatment.

This study further examined SD-associated antidepressant effects in learned helplessness behavior. We confirmed that this transition, like previously studied rapid antidepressant effects on depressive-like behavior[11,49,60,63,76], involves changes in dopamine release in mPFC for initiation and Drd1-mediated changes in excitatory synapse neuroplasticity for maintenance. Together, these data demonstrate shared dopamine-dependent neuroplasticity mechanisms in bidirectional affective transitions. Future investigations are required to understand the functional significance of changes to discrete classes of dopamine transients after brief sleep deprivation and to determine whether neuroplasticity changes in other brain regions, as in the mPFC, also serve to define the temporal window for maintaining an affective state after a given transition.

Notably, the current investigation, while linking the induction of a cluster of changes in affective states to restructuring dopaminergic dynamics in distributed neural systems and mPFC neuroplasticity, remains far from a complete model of bipolar disorder. Nevertheless, we propose that a framework focusing specifically on affective state lability may provide a path toward developing rodent models relevant to understanding aspects of bipolar disorder. Many behavioral effects we observed after acute SD were transient, lasting on average 24 hrs or less, with the sole exception of improvement in the learned helplessness task. It remains to be determined whether BD-linked pathological backgrounds or repeated experiences with sleep perturbation are associated with longer-lasting affective states via the mechanisms described here, given prior reports linking BD to the sensitivity of DA signaling across one or multiple projection pathways[15,36,77,78]. Further elaborating the causal relationship between dopamine, neuroplasticity, and behavioral state transitions may provide mechanistic insights into the pathophysiology of affective disorders and pave the path to developing new antidepressants and mood stabilizers.

STAR METHODS

RESOURCE AVAILABILITY

Lead contact—Further information and requests for resources and reagents should be directed to and will be fulfilled by the Lead Contact, Yevgenia Kozorovitskiy (Yevgenia.Kozorovitskiy@northwestern.edu).

Materials availability—This study did not generate new unique reagents.

Data and code availability

- All data reported in this paper will be shared by the lead contact upon request.
- This study does not report original code.
- Any additional information required to reanalyze the data reported in this paper is available from the lead contact upon request.

EXPERIMENTAL MODEL AND STUDY PARTICIPANT DETAILS

Mouse strains and genotyping.—Animals were handled according to protocols approved by Northwestern University Animal Care and Use Committee. Weanling and adult male and female mice (postnatal days 40-120) were used in this study. Subject sex was specified in each experiment in Figure Legends. The results between sexes were not significantly different in experiments using male and female mice. All mice were group-housed, with standard feeding and 12-hour light and 12-hour dark cycle (6:00 or 7:00 lights on). Enrichment includes a plastic igloo shelter and nesting materials (nestlets). Littermates were randomly assigned to conditions. C57BL/6 mice used for breeding and backcrossing were acquired from Charles River (Wilmington, MA), and all other mouse lines were obtained from the Jackson Laboratory (Bell Harbor, ME) and bred in-house. Only healthy and immunocompetent mice were used. Mice in this study were not involved in any previous procedures.

B6.SJL-*Slc6a3*$^{tm1.1(cre)Bkmn}$/J mice which express Cre recombinase under the control of the dopamine transporter promoter, are referred to as DAT^{iCre} [79]; C57BL/6-Tg(Thy1-EGFP/SQSTM1)02Mcwo/J, which express EGFP under control of the Thy-1 promoter, are referred to as Thy1-EGFP. Drd1$^{tm2.1stl}$ floxed mutant mice that possess loxP sites flanking the single exon of the Drd1a gene, are referred to as Drd1^{ff} [80]. The Th-2A-Flpo mouse line, which expresses Flpo recombinase under the control of the Th promoter, was a gift from Dr. Rajeshwar Awatramani[55]. All transgenic animals were backcrossed to C57BL/6 for several generations. Heterozygous Cre^{+} mice were used in experiments. Standard genotyping primers are available on the Jackson Lab website.

METHOD DETAILS

Stereotactic injections and fiber implants—Conditional expression of target genes in Cre- or Flpo-containing neurons was achieved with recombinant adeno-associated viruses (AAVs) using the FLEX cassette or encoding a double-floxed inverted open reading frame (DIO or fDIO) of target genes[81]. For fiber photometry experiments in the VTA, DAT^{iCre} mice were transduced with AAV1.CAG.FLEX.GCaMP6f.WPRE-SV40 (1.33 x 10^{13} GC/ml) from the UPenn viral core (Philadelphia, PA, a gift from the Genetically Encoded Neuronal Indicator and Effector Project (GENIE) and Douglas Kim; Addgene viral prep #100835-AAV1)[82]. For photometry of DA transients, mice were transduced with AAV9.hSyn.GRAB.DA2m (1.7 x 10^{13} GC/ml, Addgene viral prep #140553-AAV9 from Dr. Yulong Li[53]). For chemogenetic experiments in VTA without projection specificity, DAT^{iCre} mice were transduced with a custom-built AAV1.CBA. DIO. hM4Di.mCherry (1.28 x 10^{13} GC/ml, Vigene Biosciences, Rockville, MD, plasmid a gift from Dr. Bernardo Sabatini)[83]. For chemogenetic experiments with projection targeting, Th-2A-Flpo mice were transduced with AAV1.CBA.DIO.hM4Di.mCherry and retroAAV.EF1a.fDIO.Cre (a gift from Esteban Engel & Alexander Nectow, Addgene viral prep #121675-AAVrg)[84]. For glutamate uncaging-evoked spinogenesis experiments and spine density measurements, AAV8.CAG.FLEX.EGFP (3.1 x 10^{12} GC/ml, UNC vector core, Dr. Ed Boyden) was co-injected with AAV1.hSyn.Cre.WPRE.hGH (1 x 10^{10}, UPenn viral core, Dr. James M. Wilson, unpublished) to achieve sparse expression in mPFC pyramidal neurons of C57BL/6 or Drd1^{ff} mice.

Neonatal viral transduction was carried out to minimize invasiveness and increase surgical efficiency[81,85-89]. P3-6 mice were cryoanesthetized, received ketoprofen for analgesia, and were placed on a cooling pad. The virus was delivered at a rate of 100 nl/min for up to 150-200 nl using an UltraMicroPump (World Precision Instruments, Sarasota, FL). The medial prefrontal cortex (mPFC) was targeted in neonates by directing the needle immediately posterior to the eyes, 0.3 mm from the midline, and 1.8 mm ventral to the skin surface. The ventral tegmental area (VTA) was targeted in the neonates by directing the needle approximately ±0.2 mm lateral from Lambda and 3.8 mm ventral to the skin surface. Coordinates were slightly adjusted based on pup age and size. Following the procedure, pups were warmed on a heating pad and returned to home cages. Mice were genotyped after the procedure prior to weaning, and Cre-negative littermates were used as controls. All other brain regions were targeted using adult intracranial injections (> P40).

For adult intracranial injections, mice were anesthetized with isoflurane (3% for induction, 1.5-2% for maintenance), received ketoprofen, meloxicam, or Buprenorphine-SR/ER for analgesia, and were placed on a small animal stereotaxic frame (David Kopf Instruments, Tujunga, CA). AAVs were delivered through a pulled glass pipette at a rate of 100-150 nl/min using an UltraMicroPump (World Precision Instruments, Sarasota, FL). Injection coordinates for VTA, 3.0 mm posterior to bregma, 0.4 mm lateral, and 4.3-4.5 mm below the pia; for SNc, 2.8 mm posterior to bregma, 1.2 mm lateral, and 4.0-4.2 mm below the pia; for mPFC, 2.3 mm anterior to bregma, 0.4 mm lateral, and 1.3-1.6 mm below the pia; for NAc, 1.7 mm anterior to bregma, 1.0 mm lateral, and 4.5 below the pia; for the hypothalamus (HA), 0.5-1 mm posterior to bregma, 0.5 mm lateral, and 4.4 below the pia. Pipettes were held at the injection location for 15 min following AAV release. Coordinates were slightly adjusted based on mouse age and size. Viral vectors were allowed to express for at least four weeks before behavioral evaluation.

For photometry fiber placement, mice were implanted with a 400 μm diameter 0.57 NA single mode optical fiber (Doric lenses, Quebec City, QC, Canada) directly above the VTA: −3.0 mm (AP); +0.4 mm (ML); −4.3 - 4.5 mm (DV); NAc: +1.7 mm (AP); +1.0 mm (ML); −4.2 mm (DV); mPFC: +2.2 mm (AP); +0.5 mm (ML); −1.5 – 2.0 mm (DV); HA: −0.5 mm (AP); +0.5 mm (ML); −4.3 mm (DV); and dStr: +0.5 mm (AP); +2.0 mm (ML); −2.2 mm (DV). Real-time photometry recording was performed during optical fiber implant optimal targeting, after prior neonatal or adult AAV transduction and expression (> 4 weeks). When the fiber tip approached the GCaMP or $GRAB_{DA}$ expression region, a continuous increase in fluorescence intensity was observed. The final position of implantation was determined by the cessation of further increases in fluorescence intensity. Mice recovered for at least 7 days after implantation before the onset of behavioral experiments.

Ovariectomy and hormone treatment—To control female receptiveness, ovariectomy was performed in sexually experienced females (P90-120) in order to artificially control the estrus stage[90]. Females were anesthetized with isoflurane and put in a prone position on a heating pad. A 1 x 3 cm region between the last rib and pelvis was shaved, and the area was disinfected. A 1 cm sagittal incision was made in the midline, and a small window (0.5 x 0.5 cm, 1 cm lateral to the midline) was made to expose the ovary, which was subsequently removed. For oviductectomy, oviducts were ligated bilaterally without the

removal of ovaries. The incision was then closed with sutures, and the animal was returned to a new cage after recovery from anesthesia. With appropriate monitoring and analgesic regimen following approved procedures, mice were singly housed until incisions were fully closed. To induce sexual receptiveness, two doses of Estradiol benzoate (EB) (10 μg in 0.05 ml corn oil) were subcutaneously injected 48 hr and 24 hr before the behavioral test, and one dose of progesterone (500 μg in 0.05 ml corn oil) was subcutaneously injected 2-4 hr before testing.

Sleep deprivation—Custom-built sleep deprivation devices were used for acute sleep deprivation. Each device consists of a clear-cast acrylic cylinder (20.3 cm outer diameter, 19.7 cm inner diameter, 30.5 cm height, McMaster-Carr), and a clear-cast acrylic circle plate (17.8 cm diameter) as the supporting base for the motor and rotating beam. A DC motor (12V) was attached to the base, and a plastic bar (0.5 cm × 0.7 cm × 17.5 cm) served as a rotating beam, with a 3D printed cuff to attach to the motor. A 3D printed platform (3 cm diameter) was placed 7 cm above the base. For free access to food and water, a stainless-steel wire mesh sheet (30.5 × 30.5 cm, McMaster-Carr) was placed on top of the device with food and a water bottle. The external cylinder wall was covered with opaque material to control environmental stimuli. Blue tape on the outside of the floor of the chamber blocked additional light leaks.

On the day of acute sleep deprivation, mice were placed in the activated sleep deprivation devices from light onset to offset (ZT 0-12), in a room with standard light illumination and temperature (~23°C). Animals had free access to food and water during the sleep deprivation period. At the end of sleep deprivation, the room light was switched to infrared illumination for further behavioral experiments. Notably, this sleep deprivation procedure involves a transition to a new environment, which can impact sleep architecture[91], a consideration partly controlled by the inclusion of a control group with a large platform (6 cm diameter). For the evaluation of different behavioral categories in the same group of animals, mice underwent each behavior test after separate SD periods with 7-10-day intervals. The order of tests and overall timeline details are in Supplementary Figure S2A.

Behavior assays—To assess the locomotor activity, mice (> P60) were placed in an open field arena under infrared illumination. Mice explored the arena for 15 min with video recording using a raspberry pi camera (25 fps). After sleep deprivation, mice were returned to their home cage for 5–10 min before the locomotion test.

Prior to the male-male social interaction test, each male mouse (P80 – 120) was cohoused with an oviductectomized female for at least one week. The bedding material was maintained for the full duration of the cohousing period. Female mice were separated from the males one day before the baseline test of male-male social interaction. After sleep deprivation, the resident mouse was returned to the home cage for a 10-minute-long accommodation period before the social interaction test. After the accommodation period, one young opponent male, weighing about 3-5 grams less than the resident, was placed in the social interaction arena for 10 minutes, with the social interaction recorded. Group-housed C57BL/6 mice younger than the tested mice but older than P70 were used as intruders.

Similar to male-male interaction, each male mouse (P80–120) was cohoused with an oviductectomized female for at least a week, and female mice were separated from the males one day before the baseline test. Instead of the young male opponent, a hormone-treated ovariectomized C57BL/6 female (P90–120) was introduced to the resident cage for a 10-minute-long social interaction test, with video recording. Only mounting, fast, and slow intromission was scored as sexual behavior. Different females were used for each male mouse across longitudinal behavioral evaluations. The males did not have paternal experience, and the females used in behavioral tests and cohousing were either ovariectomized or oviductectomized.

The learned helplessness procedure consisted of two induction sessions (1 session per day; 360 inescapable foot shocks per session; 0.3 mA, 3 sec; random 1-15 sec inter-shock intervals). Active/Passive Avoidance Shuttle Boxes from MazeEngineers (Boston, MA) were used for the experiment. To assess the behavioral state, test sessions (30 escapable foot shocks per session; 0.3 mA, 10 sec; random 5-30 sec inter-shock intervals) were conducted prior to induction, 24 hrs after the last induction session, and following acute sleep deprivation. Testing was performed in a shuttle box (18 × 18 × 20 cm) equipped with a grid floor and a door separating the two compartments. No conditioned stimulus was delivered before or after the shocks. Escapes were scored when the animal shuttled between compartments during the shock. The shock automatically terminated when the animal shuttled to the other compartment. Failures were scored when the animal failed to escape before the shock ended. All behavioral assays were conducted during the active phase of the circadian cycle.

Sucrose preference test was performed in the homecage after each LH test. Food was given ad libitum. 1% sucrose solution and water were loaded into two separate liquid diet feeding tubes with holders (Bio-Serv, cat. No. 9015 and 9019). The consumption of sucrose solution and water in the 12-hr period was measured[92]. The sucrose preference index was calculated as 100% x (Volume of consumed sucrose)/(Volume of consumed sucrose + water). Schematics of mice were made using BioRender.

PaRac1 plasmid construction—pAAV-SARE.ArcMin-PSD95(Δ1.2)-mVenus-MCS-DTE was synthesized by Genscript based on Hayashi-Takagi et al[64]. SARE.ArcMin promoter was based on Kawashima et al. (104bp synaptic activity-responsive element, - 6793 to −6690, and 421bp, −222bp to +198bp, of mouse Arc/Arg-3.1 gene)[93]. Following the promoter and a start codon (ATG), PSD-95(ΔPDZ1.2) sequence was inserted in the frame (generated by deleting the nucleotides (nts) 250 to 993 based on the numbering of NM_019621), followed by mVenus sequence. DTE sequence was taken from 2036bp to 2699bp from NM_019361. A multicloning site sequence (CGCTTAATTAAGGTACCGCTAGCGGCGCGCCGAATTC) was inserted between mVenus and DTE. PaRac1 sequence was PCR amplified from pTriEx-mVenus-PA-Rac1 (Addgene# 22007, a gift from Dr. Klaus Hahn[94]) using 5’-agctgtacaagggttctggatcc-3’, and 5’-attcggcgcgccttacaacagcaggcattttctcttc-3’, and inserted into pAAV-SARE.ArcMin-PSD95(Δ1.2)-mVenus-MCS-DTE between BsrGI and AscI MCS sites. The same additional mutations (L514K and L531E) of the LOV2 domain on PaRac1 was introduced using Q5 polymerase

mutagenesis with the following primers (5'-catgctcagttccatccttctgaaccccaataaag-3', and 5'-tccgagatgctgccgagagagagggagtcatggagattaagaaaactgcag-3') to produce the final construct pAAV-SARE.ArcMin-PSD95(Δ1.2)-mVenus-PaRac1(L514K, L531E)-DTE. PaRac1 was packaged into AAV1 by Canadian Neurophotonics Platform Viral Vector Core Facility (RRID:SCR_016477).

To modify the fluorophore for optimized fluorescent imaging, mVenus was removed from pAAV-SARE.ArcMin-PSD95(Δ1.2)-mVenus-PaRac1 by restriction digestion with BsrGI-EcoRI. The mScarlet was amplified from pCAG-FLEX-mScarlet-WPRE (a gift from Dr. Ryan Larsen, Addgene #99280) using 5'-GTGAGCAAGGGCGAGGCAGT-3' and 5'-CTTATCGTCGTCATCCTTGTAGTCCTTAATCTTGTACAGCTCGTCCATGC-3' and subcloned into pAAV-SARE.ArcMin-PSD95(Δ1.2)-PaRac1 to make pAAV-SARE.ArcMin-PSD95(Δ1.2)-mScarlet-PaRac1.

For AAV packaging of the construct, HEK293T cells were obtained from ATCC and cryo recovered in complete Dulbecco's Modified Eagle Medium (DMEM) supplemented with 10% fetal bovine serum (FBS) and 100 U/mL penicillin-streptomycin in 37°C/5% CO_2 incubator (Cat. No. 11965118, 10437028, 15140122, Thermo Fisher). AAV was prepared from HEK293T cells by triple transfection using linear 25k polyethyleneimine (Cat. No. 23966-1, Polysciences, Warrington, PA). Forty μg of total DNA per 150-mm dish (5.7 μg of pAAV, 22.8 μg of pUCmini-iCAP-PHP, and 11.4 μg of pHelper) was used. pUCmini-iCAP-PHP.eB (Addgene #103005, a gift from Dr. Viviana Gradinaru) and pHelper were purchased from Cell Biolabs, Inc. (Cat. No. 340202). Briefly, DNA was diluted in 2 ml OptiMEM (Thermo Fisher, Cat. No. 31985062). 200 μg of PEI prepared was added to the mixture, followed by vigorous vortexing. DNA-PEI complex was incubated at RT for 15 min and added dropwise to cells. On the following day, the media was changed to OptiMEM. Five days post transfection, AAV-containing media was filtered using a 45 μm filter, aliquoted, and stored at −80°C. Crude adeno-associated viral preparation was used to perform primary neuronal transduction and in vivo expression validation.

Primary cortical neuron cultures—Cortical neurons were harvested from mouse embryos euthanized at embryonic day 15-17. Embryonic brains were dissected in ice-cold dissection media (Hank's balance salt solution HBSS, 2% penicillin-streptomycin, 20 mM HEPES). Meninges were removed from each brain, and cortices were dissected out. The cortices were chopped into small pieces using microscissors and pooled in 5 mL dissection media containing 0.25% trypsin and 0.1% DNaseI and trypsinized at 37°C for 20-25 min. Cortices were washed twice with warm dissection media and once with warm plating medium (MEM, supplemented with 10% heat-inactivated horse serum, 0.6% glucose, 1 mM Na pyruvate, 1% Glutamax, 1% penicillin-streptomycin) for 5 min each. Tissues were titrated into single-cell suspension in 3 mL fresh plating medium with unpolished and, subsequently, polished glass Pasteur pipettes. 80,000 cells were plated in 12 well plates containing poly-D-lysine coated 17 mm coverglass. After 12 hrs of seeding, plating media was removed from each well and replaced with complete neurobasal media (neurobasal supplemented with 1% B27, 1% Glutamax, and 0.5% penicillin-streptomycin). Subsequently, approximately 50% of the media in each well was replaced with fresh

complete neurobasal media every three days. Neurons were maintained at 37 °C under 5% CO_2 until the experimental end point.

At DIV3, neurons were transduced with pAAV-paRac1, AAV1-hSyn-Cre-WPRE-hGH (Penn vector core #AV-1-PV2676), and AAV8-FLEX-GFP (UNC core) for 12 hrs, after which the media was completely replaced with fresh conditioned neurobasal media. Neurons were maintained until DIV21 for pharmacological manipulations. For activity induction, DIV21 cortical neurons were incubated with neurobasal media containing 1μM Forskolin (Tocris, 1099) and 0.1% DMSO as control for 16 hrs. Then, cells were harvested for immunoprecipitation and immunocytochemistry.

PaRac1-Pak1 affinity assay—DIV 3 neurons were transduced with PaRac1-mScarlet and divided into light stimulation and dark. At DIV21, after pharmacological treatment (DMSO-0.1% and FSK- 1μM for 16 hrs) the cells in the light stimulation group were exposed to white fluorescent light (750 mW for one well of a six well plate; −4.21 W/cm^2) for 10 min and the dark group was incubated in a dark room with red light illumination to avoid PaRac1 activation. Cells were washed with Phosphate buffer saline twice and collected using a cell scraper. Cells were pelleted at 1200G and lysed in ice-cold lysis buffer provided in the Rac1 activation magnetic beads pulldown assay kit (Millipore, Cat No#17-10393) and protein inhibitor cocktail (Complete; Roche Diagnostics, Indianapolis, IN). Lysates were pulse sonicated intermittently on ice, with cell debris cleared by centrifugation. The soluble fraction was split into positive, negative control, and IP samples based on the protein concentration. Rac1 pull-down assay was performed using the directions from the kit.

Western blot analysis—IP samples collected from Rac1 pulldown were separated into 12% Tris-glycine gels and transferred to nitrocellulose membrane (Cat. No. 926-31090, LI-COR, NE, USA). Blots were briefly rinsed with Tris-buffered saline (TBS). Total protein was detected using REVERT 700 according to the manufacturer's instructions. For detecting individual proteins, unless specified, blots were blocked with 5% milk-TBST (0.1% Tween-20) for 1 hr at RT. Primary antibodies were added in the same blocking buffer for overnight incubation (1:1,000 rabbit RFP, Rockland, 600-401-379, and 1:1,000 mouse anti-Rac1 clone 23A8, provided in the kit). All secondary antibodies were purchased from Li-COR and used at 1:10,000 in TBST for 1 hr at RT. Blots were washed three times after secondary antibody incubation for 10 min each with TBST. Blots were scanned using an LI-COR Odyssey CLx scanner at the same intensity and threshold. All quantification was performed using LI-COR Image Studio version 5.2. For densitometry quantification, band signals after background correction were normalized to total protein stains in each blot.

Photostimulation of PaRac1 in vivo—Mice were virally transduced with SARE.ArcMin-PSD95(Δ1.2)-mVenus-PaRac1(L514K, L531E)-DTE bilaterally into mPFC. Two weeks after viral transduction, mice were implanted with a bilateral single-mode optical fiber (200 μm diameter, 0.48 NA, Doric lenses, Quebec City, QC, Canada) directly above the mPFC: +2.2 mm (AP); ±0.4 mm (ML); −1.5 mm (DV). For photoactivation in behavioral experiments, mice were stimulated with continuous illumination at 470 nm (M470F3, Thorlabs, Newton, NJ), with an intensity of 5 mW at each tip of the bilateral fiber for 1 hour.

Electroencephalogram and electromyography—EEG and EMG signals were acquired using a custom-built system[95]. A headpiece with two references, four EEG, and two EMG electrodes was constructed from 100-position receptacle connectors (Digi-Key, Thief River Falls, MN). Silver wires (A-M Systems, Sequim, WA) were attached to EMG electrodes for EMG recording of back muscles. The headpiece was subsequently implanted on the brain surface of the parietal cortex, with EMG wires implanted subdermally in the back region. During recording, the headpiece was connected to a RHD2132 amplifier headstage (Intan Technologies, Los Angeles, CA), which connected with a custom-built acquisition system (Open Ephys, Atlanta, GA). Signals were recorded using an Open Ephys GUI at 1KHz. For data analyses, raw signals were band-pass filtered (0.5–50 Hz for EEG, 10–100Hz for EMG) and subsequently analyzed using an online server of Sleep Learning (Sleep Phase Identification with Neural networks for Domain-invariant LEearning, SPINDLE) at https://sleeplearning.ethz.ch, a machine learning-based algorithm for automated sleep scoring[96]. The automated sleep scoring method was validated with data in four animal cohorts across three independent sleep labs (Brown, Baumann, and Adamantidis labs) by Miladinović et al. Supplemental validation in this study is provided in Supplemental Figure S1.

Fiber photometry—Hardware was created based on open-source resources made available by Dr. Thomas Davidson[72]. A custom-built setup[50,97] was created combining Doric fluorescence mini-cube (Doric, Westport, CT) and a 2151 Femtowatt photoreceiver with a lensed adapter (Newport, Irvine, CA). All downstream hardware, including fiberoptic cannulae and patch cords, except for LEDs and drivers (Thorlabs, Newton, NJ), was acquired from Doric (Quebec, Canada). A whole-cell electrophysiology recording system (DAQ + software) was used to acquire the signal and drive the LED, with a modified version of MATLAB-based Scanimage[98] adapted for electrophysiology recordings. Signals were sampled at 1 kHz and downsampled to 40 Hz for non-time-locked analyses. The fluorescence signal was baseline adjusted for photobleaching in non-overlapping 100 sec (for GCaMP6f) or 600 sec (for $GRAB_{DA}$) windows as (signal-median(signal)) / median(signal), denoted as dF/F. Recordings were made during sleep deprivation or in the home cage at ZT6 that represents the midpoint in the acute SD paradigm. Additional analysis details are below.

Acute slice preparation and electrophysiology—Animals were deeply anesthetized by inhalation of isoflurane, followed by transcardial perfusion with ice-cold, oxygenated artificial cerebrospinal fluid (ACSF) containing (in mM) 127 NaCl, 2.5 KCl, 25 $NaHCO_3$, 1.25 NaH_2PO_4, 2.0 $CaCl_2$, 1.0 $MgCl_2$, and 25 glucose (osmolarity 310 mOsm/L). After perfusion, the brain was rapidly removed and immersed in ice-cold ACSF equilibrated with 95%O_2/5%CO_2. Tissue was blocked and transferred to a slicing chamber containing ice-cold ACSF, supported by a small block of 4% agar (Sigma-Aldrich). Bilateral 300 μm-thick slices were cut on a Leica VT1000s (Leica Biosystems, Buffalo Grove, IL) in a rostrocaudal direction and transferred into a holding chamber with ACSF, equilibrated with 95%O_2/5%CO_2. Slices were incubated at 34°C for 30 min prior to electrophysiological recording or 2-photon imaging. Slices were transferred to a recording chamber perfused with oxygenated ACSF at a flow rate of 2–4 ml/min at room temperature[81,85,99].

To assess the number of action potentials, cell-attached recordings were obtained from neurons visualized under infrared DODT or DIC contrast microscopy. Recording electrode pipettes were filled with the internal solution for voltage-clamp recordings to monitor spontaneous break-in, with pipette resistance varying between 3 and 7 MΩ. Dopaminergic neurons were identified by the expression of a fluorophore in DAT^{iCre} mice. Recording electrodes contained the following (in mM): 120 $CsMeSO_4$, 15 CsCl, 10 HEPES, 10 Na- phosphocreatine, 2 MgATP, 0.3 NaGTP, 10 QX314, and 1 EGTA (pH 7.2-7.3, ~295 mOsm/L). Recordings were made using 700B amplifiers (Axon Instruments, Union City, CA); data were sampled at 10 kHz and filtered at 4 kHz with a MATLAB-based acquisition script (MathWorks, Natick, MA). Offline analysis of electrophysiology data was performed using MATLAB (Mathworks, Natick, MA) and Clampfit (Molecular Devices, San Jose, CA).

Two-photon imaging and glutamate uncaging—Dendritic imaging and uncaging of MNI-glutamate for spinogenesis induction were accomplished on a custom-built microscope combining two-photon laser-scanning microscopy (2PLSM) and two-photon laser photoactivation[49,81,100,101]. Two mode-locked Ti:Sapphire lasers (Mai Tai eHP and Mai Tai eHP DeepSee, Spectra-Physics, Santa Clara, CA) were tuned to 910 and 725 nm for exciting EGFP and uncaging MNI-glutamate, respectively. The intensity of each laser was independently controlled by Pockels cells (Conoptics, Danbury, CT). A modified version of Scanimage software was used for data acquisition[98]. For glutamate uncaging, 2.5 mM MNI-caged-L-glutamate (Tocris) was perfused into the slice chamber, and 725 nm light guided through a galvo scanhead was used to focally release the caging group. Secondary and tertiary dendritic branches were selected for dendritic imaging and spinogenesis induction. MNI-glutamate was uncaged near the dendrite (~0.5 μm) at 2 Hz using up to eighty 1 ms-long pulses. Images were continually acquired during the induction protocol at 1 Hz, and uncaging was stopped if a spine head was visible before 80 uncaging pulses were delivered. Analysis was carried out on raw image stacks and z-projections. Successful induction of a new dendritic spine was scored when a protrusion from the dendrite in the uncaging location was observed. A newly generated dendritic spine had to satisfy the following criteria: de novo protrusion from the dendrite within 1 μm of the uncaging site; mean spine head fluorescence matching average fluorescence of spine heads on the parent dendrite; mean spine head fluorescence exceeding 20% of intensity in the parent dendrite. Changes in fluorescence intensity were profiled using line-scan analyses. For each animal, the probability of spinogenesis is represented as the fraction of successful induction trials out of all conducted trials for the individual.

Tissue processing and immunohistochemistry—Mice were deeply anesthetized with isoflurane and transcardially perfused with 4% paraformaldehyde (PFA) in 0.1 M phosphate-buffered saline (PBS). Brains were post-fixed for 1-5 days and washed in PBS, prior to sectioning at 60 μm on a vibratome (Leica Biosystems). Sections were pretreated in 0.2% Triton X-100 for an hour at RT, then blocked in 10% bovine serum albumin (BSA, Sigma-Aldrich, ST Louis, MO): PBS with 0.05% Triton X-100 for two hours at RT, and incubated for 24-48 hrs at 4°C with primary antibody solution in PBS with 0.2% Triton X-100. On the following day, tissue was rinsed in PBS, reacted with

secondary antibodies for 2 hrs at RT, rinsed again, then mounted onto Superfrost Plus slides (ThermoFisher Scientific, Waltham, MA). Sections were dried and coverslipped under ProLong Gold antifade reagent with DAPI (Molecular Probes, Life Technologies, Carlsbad, CA) or under glycerol:TBS (9:1) with Hoechst 33342 (2.5 μg/ml, ThermoFisher Scientific). Primary antibodies used in the study were rabbit anti-tyrosine hydroxylase (1:1000; AB152, Millipore, Burlington, MA), rabbit anti-RFP (1:500, 600-401-379, Rockland, Limerick, PA), and goat anti-RFP (1:500, 200-101-379, Rockland, Limerick, PA). Alexa Fluor 488-, Fluor 594-, or Fluor 647-conjugated secondary antibodies against rabbit and goat (Life Technologies, Carlsbad, CA) were diluted 1:500.

Coverslips with cells were fixed with 4% paraformaldehyde and 4% sucrose in PBS at RT for 15 min and washed three times with PBS. Samples were blocked and permeabilized with 10% bovine serum albumin 0.2% Triton-X100 in PBS for 1 hr at RT. Primary antibody incubation (anti-RFP, Rabbit, 1:1,000) was performed at 4°C overnight in 5% BSA 0.1% Triton-X100 in PBS. Samples were washed three times with 0.1% triton PBS. Secondary antibody incubation was performed at RT for 1 hr in 0.1% triton-X100 PBS (containing 50% blocking PBS buffer). Coverslips were washed three times with 0.1% triton PBS, air dried, and mounted under 10% TBS 90% glycerol mounting media (2.5 μg/ml Hoescht 33342). Whole sections were imaged with an Olympus VS120 slide scanning microscope (Olympus Scientific Solutions Americas, Waltham, MA). Dendrites and dendritic spine images were acquired with an Olympus FV3000 confocal microscope (Olympus Scientific Solutions Americas, Waltham, MA).

QUANTIFICATION AND STATISTICAL ANALYSIS

Quantification of behavior—For evaluating locomotor behavior, Toxtrac[102] was used to track the animal's position, defined by its body center, and quantify the distance traveled in each session. For evaluating social interaction, behaviors were manually annotated using Behavioral Observation Research Interactive Software (BORIS)[103]. Social behaviors were subdivided into unilateral sniffing, reciprocal sniffing, allogrooming, chasing, attacking, male-male mounting, male-female mounting, intromission, and ejaculation. Total time spent engaged in social interaction, aggression (attacking, aggressive chasing, and male-male mounting), and sexual behaviors (mounting and intromission) were calculated for comparisons among conditions.

Quantification of fiber photometry data—The heatmap of Ca^{2+} and DA transients dF/F was constructed by plotting 1,800-sec-long continuous recordings with 50-sec-long bins. Spontaneous transients were detected with templates created from an average of 10 – 20 experimenter-defined events using the template-matching algorithm built in Clampfit (Molecular Devices, San Jose, CA)[104] (Figure S5). Transients matching the kinetics of GCaMP6f and $GRAB_{DA}$ were selected to generate the templates[53,82]. In event detection template matching in pCLAMP software, the template is slid along the data trace once at a time, scaled, and offset to optimally fit the data at each point. Optimization of fit is found by minimizing the sum of squared errors (SSE) between the fitted template and the data. A detection criterion value is calculated at each position by dividing the template scaling factor by a measure of the goodness of fit (derived from the SSE). Template match threshold was

set at 1.5 based on the false detection rates reported in previous studies[105]. All sections of the trace with a detection criterion greater than or equal to 1.5 are automatically extracted as candidate events. For GCaMP6f, the dF/F of individual transients from all animals and the average dF/F from each animal were plotted. For $GRAB_{DA}$, the AUC of transients for each animal was calculated from the dF/F of positive going peaks of all automatedly detected transients in the 1,800-sec-long recordings. Peaks were omitted from analyses if they were less than 10% of the distance from minimum to maximum dF/F for the recording. The baseline was defined using the mean dF/F of the initial 20% of the transient window before the onset of the transient.

Quantification of fiber placement—Coronal slices containing fiber photometry tracts were processed using WholeBrain[106] software package in R (https://www.R-project.org/). Histological slices were analyzed and registered to the Allen Mouse Brain Common Coordinate Framework (CCFv3)[54] using the autofluorescence of coronal brain sections[107]. Sections with fiber tracts were analyzed at approximately 50 μm intervals from the entry point of the fiber tip. A total of 4 - 10 coronal slice images were analyzed per mouse brain, and fiber tips at 1 - 2 bregma coordinates were plots for each animal. Fiber placement for each brain section was denoted at the most ventral-medial location where the fiber tract was observed. Medial-lateral and dorsal-ventral coordinates registered to the CCFv3 were obtained for each section and plotted on a representative coronal section using the WholeBrain package.

Quantification of fluorescence expression—Two-dimensional quantitative tracking of dopamine cell expression in DAT^{iCre} mice and retrograde axonal projections (Th-Flpo mice) were performed using an adapted version of the open-source software package, Wholebrain. Autofluorescence of coronal brain sections is used to register slices to the Allen Mouse Brain CCFv3, and segmented axonal and somatic signals are transformed to the reference brain section. Our modified package implemented a Sobel edge-detection method to identify axonal processes and multi-otsu thresholding to segment somatic signals in coronal sections collected at a 150 μm sampling interval. Segmented axons were quantified as pixel counts for each registered brain region, and each sample was normalized to total axonal content to account for variability in viral expression across samples. To calculate relative label density, total pixel counts were normalized to the surface area (mm^2) of each region of interest. Axonal coronal heatmaps and somatic signal visualizations were generated in R using the ‘tidyverse’ and ‘ggplot2’ packages[108].

Quantification of dendritic spine density—Sections of mPFC were imaged using a custom-built 2PLSM as described above for glutamate-evoked spinogenesis. Distal apical dendritic segments were selected for analysis. For each dendritic segment, dendritic spines were analyzed using the Dendritic Spine Counter plugin in FIJI (developed by M. Voloshin, Mighty Data, Inc., Weaverville, NC). Dendritic spine density was averaged from 8-12 dendritic segments for each animal.

Statistical analyses—Required sample sizes were estimated based on previous publications and experience. The number of biological replicates was reported, and several

internal replications are present in the study. No data were excluded after analyses. Selection criteria for aggressive behavior were as described in the results. Animals were randomly assigned to treatment groups. Group statistical analyses were done using GraphPad Prism 7 and 8 software (GraphPad, LaJolla, CA). For N sizes, the number of trials or cells recorded, as well as the number of animals, are provided in Figure legends. All data are expressed as mean ± SEM or individual plots. Probabilities are expressed as aggregate probabilities within individuals. For two-group comparisons, statistical significance was determined by two-tailed Student's t-tests. For multiple group comparisons, one-way or two-way analysis of variance (ANOVA) tests were used for normally distributed data, followed by post hoc analyses. For non-normally distributed data, non-parametric tests for the appropriate group numbers were used, as noted in the legends. $p < 0.05$ was considered statistically significant.

Supplementary Material

Refer to Web version on PubMed Central for supplementary material.

ACKNOWLEDGMENTS

The authors thank Lindsey Butler for mouse colony management and Jianyu Gu for generating EEG power spectra. This work was supported by the 2021 One Mind Nick LeDeit Rising Star Research Award, BD^2: Breakthrough Discoveries for thriving with Bipolar Disorder, R01NS107539, R01MH117111, Rita Allen Foundation Scholar Award (Y.K.). M.W was the Christina Enroth-Cugell and David Cugell Fellow and affiliated with T32AG20506. V.D. was a fellow of the American Heart Association (19PRE34380056) and affiliated with 2T32GM15538.

INCLUSION AND DIVERSITY

We support inclusive, diverse, and equitable conduct of research.

REFERENCES

1. Davidson RJ (1998). Affective Style and Affective Disorders: Perspectives from Affective Neuroscience. Cogn. Emot 12, 307–330. 10.1080/026999398379628.
2. Vos T, Barber RM, Bell B, Bertozzi-Villa A, Biryukov S, Bolliger I, Charlson F, Davis A, Degenhardt L, Dicker D, et al. (2015). Global, regional, and national incidence, prevalence, and years lived with disability for 301 acute and chronic diseases and injuries in 188 countries, 1990–2013: a systematic analysis for the Global Burden of Disease Study 2013. Lancet 386, 743–800. 10.1016/S0140-6736(15)60692-4. [PubMed: 26063472]
3. Belmaker RH, and Agam G (2008). Major Depressive Disorder. N. Engl. J. Med 358, 55–68. 10.1056/NEJMra073096. [PubMed: 18172175]
4. Belmaker RH (2004). Bipolar Disorder. N. Engl. J. Med 351, 476–486. 10.1056/NEJMra035354. [PubMed: 15282355]
5. Grande I, Berk M, Birmaher B, and Vieta E (2016). Bipolar disorder. Lancet 387, 1561–1572. 10.1016/S0140-6736(15)00241-X. [PubMed: 26388529]
6. Phillips ML, and Kupfer DJ (2013). Bipolar disorder diagnosis: challenges and future directions. Lancet 381, 1663–1671. 10.1016/S0140-6736(13)60989-7. [PubMed: 23663952]
7. Kanning MK, Ebner-Priemer UW, and Schlicht WM (2013). How to Investigate Within-Subject Associations between Physical Activity and Momentary Affective States in Everyday Life: A Position Statement Based on a Literature Overview. Front. Psychol 4. 10.3389/fpsyg.2013.00187.
8. Jean-Louis G, Von Gizycki H, Zizi F, and Nunes J (1998). Mood States and Sleepiness in College Students: Influences of Age, Sex, Habitual Sleep, and Substance Use. Percept. Mot. Skills 87, 507–512. 10.2466/pms.1998.87.2.507. [PubMed: 9842593]

9. D'Mello S, and Graesser A (2012). Dynamics of affective states during complex learning. Learn. Instr 22, 145–157. 10.1016/j.learninstruc.2011.10.001.
10. McHugh RK, and Kneeland ET (2019). Affective vulnerability in substance use disorders. Curr. Opin. Psychol 30, 54–58. 10.1016/j.copsyc.2019.01.011. [PubMed: 30851660]
11. Parekh PK, Johnson SB, and Liston C (2022). Synaptic Mechanisms Regulating Mood State Transitions in Depression. Annu. Rev. Neurosci 45, 581–601. 10.1146/annurev-neuro-110920-040422. [PubMed: 35508195]
12. Wehr TA, Sack DA, and Rosenthal NE (1987). Sleep reduction as a final common pathway in the genesis of mania. Am. J. Psychiatry 144, 201–204. 10.1176/ajp.144.2.201. [PubMed: 3812788]
13. Peet M, and Peters S (1995). Drug-Induced Mania. Drug Saf. 12, 146–153. 10.2165/00002018-199512020-00007. [PubMed: 7766338]
14. McClung CA, Sidiropoulou K, Vitaterna M, Takahashi JS, White FJ, Cooper DC, and Nestler EJ (2005). Regulation of dopaminergic transmission and cocaine reward by the Clock gene. Proc. Natl. Acad. Sci 102, 9377–9381. 10.1073/pnas.0503584102. [PubMed: 15967985]
15. Mukherjee S, Coque L, Cao J-L, Kumar J, Chakravarty S, Asaithamby A, Graham A, Gordon E, Enwright JF, DiLeone RJ, et al. (2010). Knockdown of Clock in the Ventral Tegmental Area Through RNA Interference Results in a Mixed State of Mania and Depression-Like Behavior. Biol. Psychiatry 68, 503–511. 10.1016/j.biopsych.2010.04.031. [PubMed: 20591414]
16. Scott MR, and McClung CA (2021). Circadian Rhythms in Mood Disorders. Adv. Exp. Med. Biol 1344, 153–168. 10.1007/978-3-030-81147-1_9/COVER. [PubMed: 34773231]
17. Radley JJ, Rocher AB, Miller M, Janssen WGM, Liston C, Hof PR, McEwen BS, and Morrison JH (2006). Repeated stress induces dendritic spine loss in the rat medial prefrontal cortex. Cereb. Cortex 16, 313–320. 10.1093/cercor/bhi104. [PubMed: 15901656]
18. Kang HJ, Voleti B, Hajszan T, Rajkowska G, Stockmeier CA, Licznerski P, Lepack A, Majik MS, Jeong LS, Banasr M, et al. (2012). Decreased expression of synapse-related genes and loss of synapses in major depressive disorder. Nat. Med 18, 1413–1417. 10.1038/nm.2886. [PubMed: 22885997]
19. Roybal K, Theobold D, Graham A, DiNieri JA, Russo SJ, Krishnan V, Chakravarty S, Peevey J, Oehrlein N, Birnbaum S, et al. (2007). Mania-like behavior induced by disruption of CLOCK. Proc. Natl. Acad. Sci 104, 6406–6411. 10.1073/pnas.0609625104. [PubMed: 17379666]
20. McClung CA (2007). Circadian genes, rhythms and the biology of mood disorders. Pharmacol. Ther114, 222–232. 10.1016/j.pharmthera.2007.02.003. [PubMed: 17395264]
21. Li B, Piriz J, Mirrione M, Chung C, Proulx CD, Schulz D, Henn F, and Malinow R (2011). Synaptic potentiation onto habenula neurons in the learned helplessness model of depression. Nature 470, 535–541. 10.1038/nature09742. [PubMed: 21350486]
22. Ford DE, and Cooper-Patrick L (2001). Sleep disturbances and mood disorders: An epidemiologic perspective. Depress. Anxiety 14, 3–6. 10.1002/da.1041. [PubMed: 11568977]
23. Armitage R. (2007). Sleep and circadian rhythms in mood disorders. Acta Psychiatr. Scand 115, 104–115. 10.1111/j.1600-0447.2007.00968.X.
24. Xu N, Shinohara K, Saunders KEA, Geddes JR, and Cipriani A (2021). Effect of lithium on circadian rhythm in bipolar disorder: A systematic review and meta-analysis. Bipolar Disord. 23, 445–453. 10.1111/bdi.13070. [PubMed: 33650218]
25. McClung CA (2013). How Might Circadian Rhythms Control Mood? Let Me Count the Ways… Biol. Psychiatry 14, 242–249. 10.1016/j.biopsych.2013.02.019.
26. Jackson A, Cavanagh J, and Scott J (2003). A systematic review of manic and depressive prodromes. J. Affect. Disord 14, 209–217. 10.1016/S0165-0327(02)00266-5.
27. Colombo C, Benedetti F, Barbini B, Campori E, and Smeraldi E (1999). Rate of switch from depression into mania after therapeutic sleep deprivation in bipolar depression. Psychiatry Res. 86, 267–270. 10.1016/S0165-1781(99)00036-0. [PubMed: 10482346]
28. Wu JC, Kelsoe JR, Schachat C, Bunney BG, DeModena A, Golshan S, Gillin JC, Potkin SG, and Bunney WE (2009). Rapid and Sustained Antidepressant Response with Sleep Deprivation and Chronotherapy in Bipolar Disorder. Biol. Psychiatry 66, 298–301. 10.1016/j.biopsych.2009.02.018. [PubMed: 19358978]

29. Benedetti F, Fresi F, Maccioni P, and Smeraldi E (2008). Behavioural sensitization to repeated sleep deprivation in a mice model of mania. Behav. Brain Res 187, 221–227. 10.1016/j.bbr.2007.09.012. [PubMed: 17950929]
30. Young JW, Henry BL, and Geyer MA (2011). Predictive animal models of mania: hits, misses and future directions. Br. J. Pharmacol 164, 1263–1284. 10.1111/j.1476-5381.2011.01318.x. [PubMed: 21410454]
31. Gessa GL, Pani L, Fadda P, and Fratta W (1995). Sleep deprivation in the rat: an animal model of mania. Eur. Neuropsychopharmacol 5, 89–93. 10.1016/0924-977X(95)00023-1.
32. Beyer DKE, and Freund N (2017). Animal models for bipolar disorder: from bedside to the cage. Int. J. Bipolar Disord 5. 10.1186/s40345-017-0104-6.
33. Logan RW, and McClung CA (2016). Animal models of bipolar mania: The past, present and future. Neuroscience 321, 163–188. 10.1016/J.NEUROSCIENCE.2015.08.041. [PubMed: 26314632]
34. Dunlop BW, and Nemeroff CB (2007). The role of dopamine in the pathophysiology of depression. Arch. Gen. Psychiatry 64, 327–337. 10.1001/archpsyc.64.3.327. [PubMed: 17339521]
35. Dailly E, Chenu F, Renard CE, and Bourin M (2004). Dopamine, depression and antidepressants. Fundam. Clin. Pharmacol 18, 601–607. 10.1111/j.1472-8206.2004.00287.x. [PubMed: 15548230]
36. Ashok AH, Marques TR, Jauhar S, Nour MM, Goodwin GM, Young AH, and Howes OD (2017). The dopamine hypothesis of bipolar affective disorder: The state of the art and implications for treatment. Mol. Psychiatry 22, 666–679. 10.1038/mp.2017.16. [PubMed: 28289283]
37. Belujon P, and Grace AA (2017). Dopamine System Dysregulation in Major Depressive Disorders. Int. J. Neuropsychopharmacol 20, 1036–1046. 10.1093/ijnp/pyx056. [PubMed: 29106542]
38. Chaudhury D, Walsh JJ, Friedman AK, Juarez B, Ku SM, Koo JW, Ferguson D, Tsai HC, Pomeranz L, Christoffel DJ, et al. (2013). Rapid regulation of depression-related behaviours by control of midbrain dopamine neurons. Nature 493, 532–536. 10.1038/nature11713. [PubMed: 23235832]
39. Monti JM, and Monti D (2007). The involvement of dopamine in the modulation of sleep and waking. Sleep Med. Rev 11, 113–133. 10.1016/j.smrv.2006.08.003. [PubMed: 17275369]
40. Maloney KJ, Mainville L, and Jones BE (2002). c-Fos expression in dopaminergic and GABAergic neurons of the ventral mesencephalic tegmentum after paradoxical sleep deprivation and recovery. Eur. J. Neurosci 15, 774–778. 10.1046/j.1460-9568.2002.01907.x. [PubMed: 11886456]
41. Eban-Rothschild A, Rothschild G, Giardino WJ, Jones JR, and de Lecea L (2016). VTA dopaminergic neurons regulate ethologically relevant sleep–wake behaviors. Nat. Neurosci 19, 1356–1366. 10.1038/nn.4377. [PubMed: 27595385]
42. Hasegawa E, Miyasaka A, Sakurai K, Cherasse Y, Li Y, and Sakurai T (2022). Rapid eye movement sleep is initiated by basolateral amygdala dopamine signaling in mice. Science 375, 994–1000. 10.1126/SCIENCE.ABL6618/SUPPL_FILE/SCIENCE.ABL6618_MOVIES_S1_AND_S2.ZIP. [PubMed: 35239361]
43. Parekh PK, Ozburn AR, and McClung CA (2015). Circadian clock genes: Effects on dopamine, reward and addiction. Alcohol 49, 341–349. 10.1016/j.alcohol.2014.09.034. [PubMed: 25641765]
44. Spencer S, Torres-Altoro MI, Falcon E, Arey R, Marvin M, Goldberg M, Bibb JA, and McClung CA (2012). A mutation in CLOCK leads to altered dopamine receptor function. J. Neurochem 123, 124–134. 10.1111/j.1471-4159.2012.07857.x. [PubMed: 22757753]
45. Coque L, Mukherjee S, Cao JL, Spencer S, Marvin M, Falcon E, Sidor MM, Birnbaum SG, Graham A, Neve RL, et al. (2011). Specific role of VTA dopamine neuronal firing rates and morphology in the reversal of anxiety-related, but not depression-related behavior in the clockδ19 mouse model of mania. Neuropsychopharmacology 36, 1478–1488. 10.1038/npp.2011.33. [PubMed: 21430648]
46. Spencer S, Falcon E, Kumar J, Krishnan V, Mukherjee S, Birnbaum SG, and McClung CA (2013). Circadian genes Period 1 and Period 2 in the nucleus accumbens regulate anxiety-related behavior. Eur. J. Neurosci 37, 242–250. 10.1111/ejn.12010. [PubMed: 23039899]
47. Hines DJ, Schmitt LI, Hines RM, Moss SJ, and Haydon PG (2013). Antidepressant effects of sleep deprivation require astrocyte-dependent adenosine mediated signaling. Transl. Psychiatry 3, e212–e212. 10.1038/tp.2012.136. [PubMed: 23321809]

48. Chourbaji S, Zacher C, Sanchis-Segura C, Dormann C, Vollmayr B, and Gass P (2005). Learned helplessness: Validity and reliability of depressive-like states in mice. Brain Res. Protoc 16, 70–78. 10.1016/j.brainresprot.2005.09.002.
49. Wu M, Minkowicz S, Dumrongprechachan V, Hamilton P, and Kozorovitskiy Y (2021). Ketamine Rapidly Enhances Glutamate-Evoked Dendritic Spinogenesis in Medial Prefrontal Cortex Through Dopaminergic Mechanisms. Biol. Psychiatry 89, 1096–1105. 10.1016/j.biopsych.2020.12.022. [PubMed: 33637303]
50. Wu M, Minkowicz S, Dumrongprechachan V, Hamilton P, Xiao L, and Kozorovitskiy Y (2021). Attenuated dopamine signaling after aversive learning is restored by ketamine to rescue escape actions. Elife 10, e64041. 10.7554/eLife.64041. [PubMed: 33904412]
51. Roth BL (2016). DREADDs for Neuroscientists. Neuron 89, 683–694. 10.1016/j.neuron.2016.01.040. [PubMed: 26889809]
52. Morales M, and Margolis EB (2017). Ventral tegmental area: Cellular heterogeneity, connectivity and behaviour. Nat. Rev. Neurosci 18, 73–85. 10.1038/nrn.2016.165. [PubMed: 28053327]
53. Sun F, Zeng J, Jing M, Zhou J, Feng J, Owen SF, Luo Y, Li F, Wang H, Yamaguchi T, et al. (2018). A Genetically Encoded Fluorescent Sensor Enables Rapid and Specific Detection of Dopamine in Flies, Fish, and Mice. Cell 174, 481–496.e19. 10.1016/j.cell.2018.06.042. [PubMed: 30007419]
54. Wang Q, Ding SL, Li Y, Royall J, Feng D, Lesnar P, Graddis N, Naeemi M, Facer B, Ho A, et al. (2020). The Allen Mouse Brain Common Coordinate Framework: A 3D Reference Atlas. Cell 181, 936. 10.1016/J.CELL.2020.04.007. [PubMed: 32386544]
55. Poulin J-F, Caronia G, Hofer C, Cui Q, Helm B, Ramakrishnan C, Chan CS, Dombeck DA, Deisseroth K, and Awatramani R (2018). Mapping projections of molecularly defined dopamine neuron subtypes using intersectional genetic approaches. Nat. Neurosci 21, 1260–1271. 10.1038/S41593-018-0203-4. [PubMed: 30104732]
56. Beier KT, Steinberg EE, DeLoach KE, Xie S, Miyamichi K, Schwarz L, Gao XJ, Kremer EJ, Malenka RC, and Luo L (2015). Circuit Architecture of VTA Dopamine Neurons Revealed by Systematic Input-Output Mapping. Cell 162, 622–634. 10.1016/J.CELL.2015.07.015. [PubMed: 26232228]
57. Zhang SX, Lutas A, Yang S, Diaz A, Fluhr H, Nagel G, Gao S, and Andermann ML (2021). Hypothalamic dopamine neurons motivate mating through persistent cAMP signalling. Nature 597, 245–249. 10.1038/S41586-021-03845-0. [PubMed: 34433964]
58. Mcelvain LE, Chen Y, Moore JD, Lim BK, Costa RM, and Kleinfeld D (2021). Specific populations of basal ganglia output neurons target distinct brain stem areas while collateralizing throughout the diencephalon In brief. Neuron 109. 10.1016/j.neuron.2021.03.017.
59. Aleksandrova LR, and Phillips AG (2021). Neuroplasticity as a convergent mechanism of ketamine and classical psychedelics. Trends Pharmacol. Sci 42, 929–942. 10.1016/J.TIPS.2021.08.003. [PubMed: 34565579]
60. Shao LX, Liao C, Gregg I, Davoudian PA, Savalia NK, Delagarza K, and Kwan AC (2021). Psilocybin induces rapid and persistent growth of dendritic spines in frontal cortex in vivo. Neuron 109, 2535–2544.e4. 10.1016/J.NEURON.2021.06.008. [PubMed: 34228959]
61. Ali F, Gerhard DM, Sweasy K, Pothula S, Pittenger C, Duman RS, and Kwan AC (2020). Ketamine disinhibits dendrites and enhances calcium signals in prefrontal dendritic spines. Nat. Commun 11, 1–15. 10.1038/s41467-019-13809-8. [PubMed: 31911652]
62. Belujon P, and Grace AA (2014). Restoring mood balance in depression: Ketamine reverses deficit in dopamine-dependent synaptic plasticity. Biol. Psychiatry 76, 927–936. 10.1016/j.biopsych.2014.04.014. [PubMed: 24931705]
63. Moda-Sava RN, Murdock MH, Parekh PK, Fetcho RN, Huang BS, Huynh TN, Witztum J, Shaver DC, Rosenthal DL, Alway EJ, et al. (2019). Sustained rescue of prefrontal circuit dysfunction by antidepressant-induced spine formation. Science 364, eaat8078. 10.1126/science.aat8078. [PubMed: 30975859]
64. Hayashi-Takagi A, Yagishita S, Nakamura M, Shirai F, Wu YI, Loshbaugh AL, Kuhlman B, Hahn KM, and Kasai H (2015). Labelling and optical erasure of synaptic memory traces in the motor cortex. Nature 525, 333–338. 10.1038/nature15257. [PubMed: 26352471]

65. Schacher S, Castellucci VF, and Kandel ER (1988). cAMP Evokes Long-Term Facilitation in Aplysia Sensory Neurons That Requires New Protein Synthesis. Science 240, 1667–1669. 10.1126/science.2454509. [PubMed: 2454509]
66. Lammel S, Lim BK, and Malenka RC (2014). Reward and aversion in a heterogeneous midbrain dopamine system. Neuropharmacology 76, 351–359. 10.1016/j.neuropharm.2013.03.019. [PubMed: 23578393]
67. Pierce RC, and Kumaresan V (2006). The mesolimbic dopamine system: The final common pathway for the reinforcing effect of drugs of abuse? Neurosci. Biobehav. Rev 30, 215–238. 10.1016/j.neubiorev.2005.04.016. [PubMed: 16099045]
68. Gunaydin LA, Grosenick L, Finkelstein JC, Kauvar IV, Fenno LE, Adhikari A, Lammel S, Mirzabekov JJ, Airan RD, Zalocusky KA, et al. (2014). Natural Neural Projection Dynamics Underlying Social Behavior. Cell 157, 1535–1551. 10.1016/J.CELL.2014.05.017. [PubMed: 24949967]
69. Pereira Luppi M, Azcorra M, Caronia-Brown G, Poulin J-F, Gaertner Z, Gatica S, Moreno-Ramos OA, Nouri N, Dubois M, Ma YC, et al. (2021). Sox6 expression distinguishes dorsally and ventrally biased dopamine neurons in the substantia nigra with distinctive properties and embryonic origins. Cell Rep. 37, 109975. 10.1016/j.celrep.2021.109975. [PubMed: 34758317]
70. Gaertner Z, Azcorra M, Dombeck DA, and Awatramani R (2022). Molecular heterogeneity in the substantia nigra: A roadmap for understanding PD motor pathophysiology. Neurobiol. Dis 175, 105925. 10.1016/j.nbd.2022.105925. [PubMed: 36372290]
71. Poulin J-F, Zou J, Drouin-Ouellet J, Kim K-YA, Cicchetti F, and Awatramani RB (2014). Defining Midbrain Dopaminergic Neuron Diversity by Single-Cell Gene Expression Profiling. Cell Rep. 9, 930–943. 10.1016/j.celrep.2014.10.008. [PubMed: 25437550]
72. Lerner TN, Shilyansky C, Davidson TJ, Evans KE, Beier KT, Zalocusky KA, Crow AK, Malenka RC, Luo L, Tomer R, et al. (2015). Intact-Brain Analyses Reveal Distinct Information Carried by SNc Dopamine Subcircuits. Cell 162, 635–647. 10.1016/j.cell.2015.07.014. [PubMed: 26232229]
73. da Silva JA, Tecuapetla F, Paixão V, and Costa RM (2018). Dopamine neuron activity before action initiation gates and invigorates future movements. Nature 554, 244–248. 10.1038/nature25457. [PubMed: 29420469]
74. Howe MW, and Dombeck DA (2016). Rapid signalling in distinct dopaminergic axons during locomotion and reward. Nature 535, 505–510. 10.1038/nature18942. [PubMed: 27398617]
75. Azcorra M, Gaertner Z, Davidson C, He Q, Kim H, Nagappan S, Hayes CK, Ramakrishnan C, Fenno L, Kim YS, et al. (2023). Unique functional responses differentially map onto genetic subtypes of dopamine neurons. Nat. Neurosci, 1–13. 10.1038/s41593-023-01401-9.
76. Wu H, Savalia NK, and Kwan AC (2021). Ketamine for a Boost of Neural Plasticity: How, but Also When? Biol. Psychiatry 89, 1030–1032. 10.1016/j.biopsych.2021.03.014. [PubMed: 34016377]
77. Malhi GS, Tanious M, Das P, Coulston CM, and Berk M (2013). Potential mechanisms of action of lithium in bipolar disorder: Current understanding. CNS Drugs 27, 135–153. 10.1007/s40263-013-0039-0. [PubMed: 23371914]
78. Sidor MM, Spencer SM, Dzirasa K, Parekh PK, Tye KM, Warden MR, Arey RN, Enwright JF, Jacobsen JPR, Kumar S, et al. (2015). Daytime spikes in dopaminergic activity drive rapid mood-cycling in mice. Mol. Psychiatry 20, 1406–1419. 10.1038/mp.2014.167. [PubMed: 25560763]
79. Bäckman CM, Malik N, Zhang YJ, Shan L, Grinberg A, Hoffer BJ, Westphal H, and Tomac AC (2006). Characterization of a mouse strain expressing Cre recombinase from the 3′ untranslated region of the dopamine transporter locus. Genesis 44, 383–390. 10.1002/dvg.20228. [PubMed: 16865686]
80. Sariñana J, Kitamura T, Künzler P, Sultzman L, and Tonegawa S (2014). Differential roles of the dopamine 1-class receptors, D1R and D5R, in hippocampal dependent memory. Proc. Natl. Acad. Sci. U. S. A 111, 8245–8250. 10.1073/pnas.1407395111. [PubMed: 24843151]
81. Kozorovitskiy Y, Peixoto R, Wang W, Saunders A, and Sabatini BL (2015). Neuromodulation of excitatory synaptogenesis in striatal development. Elife 4, e10111. 10.7554/eLife.10111. [PubMed: 26551563]

82. Chen T-W, Wardill TJ, Sun Y, Pulver SR, Renninger SL, Baohan A, Schreiter ER, Kerr RA, Orger MB, Jayaraman V, et al. (2013). Ultrasensitive fluorescent proteins for imaging neuronal activity. Nature 499, 295–300. 10.1038/nature12354. [PubMed: 23868258]
83. Hou XH, Hyun M, Taranda J, Huang KW, Todd E, Feng D, Atwater E, Croney D, Zeidel ML, Osten P, et al. (2016). Central Control Circuit for Context-Dependent Micturition. Cell 167, 73–86.e12. 10.1016/j.cell.2016.08.073. [PubMed: 27662084]
84. Schneeberger M, Parolari L, Das Banerjee T, Bhave V, Wang P, Patel B, Topilko T, Wu Z, Choi CHJ, Yu X, et al. (2019). Regulation of Energy Expenditure by Brainstem GABA Neurons. Cell 178, 672–685.e12. 10.1016/j.cell.2019.05.048. [PubMed: 31257028]
85. Kozorovitskiy Y, Saunders A, Johnson CA, Lowell BB, and Sabatini BL (2012). Recurrent network activity drives striatal synaptogenesis. Nature 485, 646–650. 10.1038/nature11052. [PubMed: 22660328]
86. Peixoto RT, Wang W, Croney DM, Kozorovitskiy Y, and Sabatini BL (2016). Early hyperactivity and precocious maturation of corticostriatal circuits in Shank3B−/− mice. Nat. Neurosci 19, 716–724. 10.1038/nn.4260. [PubMed: 26928064]
87. Bariselli S, Tzanoulinou S, Glangetas C, Prévost-Solié C, Pucci L, Viguié J, Bezzi P, O'Connor EC, Georges F, Lüscher C, et al. (2016). SHANK3 controls maturation of social reward circuits in the VTA. Nat. Neurosci 19, 926–934. 10.1038/nn.4319. [PubMed: 27273769]
88. He CX, Arroyo ED, Cantu DA, Goel A, and Portera-Cailliau C (2018). A Versatile Method for Viral Transfection of Calcium Indicators in the Neonatal Mouse Brain. Front. Neural Circuits 12. 10.3389/fncir.2018.00056.
89. Yang Y, Wu M, Wegener AJ, Vázquez-Guardado A, Efimov AI, Lie F, Wang T, Ma Y, Banks A, Li Z, et al. (2022). Preparation and use of wireless reprogrammable multilateral optogenetic devices for behavioral neuroscience. Nat. Protoc 17, 1073–1096. 10.1038/s41596-021-00672-5. [PubMed: 35173306]
90. Ström JO, Theodorsson A, Ingberg E, Isaksson I-M, and Theodorsson E (2012). Ovariectomy and 17β-estradiol Replacement in Rats and Mice: A Visual Demonstration. J. Vis. Exp, e4013. 10.3791/4013. [PubMed: 22710371]
91. Eban-Rothschild A, Appelbaum L, and de Lecea L (2018). Neuronal Mechanisms for Sleep/Wake Regulation and Modulatory Drive. Neuropsychopharmacology 43, 937–952. 10.1038/npp.2017.294. [PubMed: 29206811]
92. Liu M-Y, Yin C-Y, Zhu L-J, Zhu X-H, Xu C, Luo C-X, Chen H, Zhu D-Y, and Zhou Q-G (2018). Sucrose preference test for measurement of stress-induced anhedonia in mice. Nat. Protoc 13, 1686–1698. 10.1038/s41596-018-0011-z. [PubMed: 29988104]
93. Kawashima T, Okuno H, Nonaka M, Adachi-Morishima A, Kyo N, Okamura M, Takemoto-Kimura S, Worley PF, and Bito H (2009). Synaptic activity-responsive element in the Arc / Arg3.1 promoter essential for synapse-to-nucleus signaling in activated neurons. Proc. Natl. Acad. Sci 106, 316–321. 10.1073/pnas.0806518106. [PubMed: 19116276]
94. Wu YI, Frey D, Lungu OI, Jaehrig A, Schlichting I, Kuhlman B, and Hahn KM (2009). A genetically encoded photoactivatable Rac controls the motility of living cells. Nat. 2009 4617260 461, 104–108. 10.1038/nature08241.
95. Wasilczuk AZ, Proekt A, Kelz MB, and McKinstry-Wu AR (2016). High-density Electroencephalographic Acquisition in a Rodent Model Using Low-cost and Open-source Resources. J. Vis. Exp 2016, e54908. 10.3791/54908.
96. Miladinović Đ, Muheim C, Bauer S, Spinnler A, Noain D, Bandarabadi M, Gallusser B, Krummenacher G, Baumann C, Adamantidis A, et al. (2019). SPINDLE: End-to-end learning from EEG/EMG to extrapolate animal sleep scoring across experimental settings, labs and species. PLOS Comput. Biol 15, e1006968. 10.1371/journal.pcbi.1006968. [PubMed: 30998681]
97. Priest MF, Freda SN, Rieth IJ, Badong D, Dumrongprechachan V, and Kozorovitskiy Y (2023). Peptidergic and functional delineation of the Edinger-Westphal nucleus. Cell Rep. 42, 112992. 10.1016/j.celrep.2023.112992. [PubMed: 37594894]
98. Pologruto TA, Sabatini BL, and Svoboda K (2003). ScanImage: Flexible software for operating laser scanning microscopes. Biomed. Eng. Online 2, 13. 10.1186/1475-925X-2-13. [PubMed: 12801419]

99. Xiao L, Priest MF, Nasenbeny J, Lu T, and Kozorovitskiy Y (2017). Biased Oxytocinergic Modulation of Midbrain Dopamine Systems. Neuron 95, 368–384.e5. 10.1016/j.neuron.2017.06.003. [PubMed: 28669546]

100. Banala S, Arvin MC, Bannon NM, Jin X-T, Macklin JJ, Wang Y, Peng C, Zhao G, Marshall JJ, Gee KR, et al. (2018). Photoactivatable drugs for nicotinic optopharmacology. Nat. Methods 15, 347–350. 10.1038/nmeth.4637. [PubMed: 29578537]

101. Xiao L, Priest MF, and Kozorovitskiy Y (2018). Oxytocin functions as a spatiotemporal filter for excitatory synaptic inputs to VTA dopamine neurons. Elife 7, e33892. 10.7554/eLife.33892. [PubMed: 29676731]

102. Rodriguez A, Zhang H, Klaminder J, Brodin T, Andersson PL, and Andersson M (2018). ToxTrac : A fast and robust software for tracking organisms. Methods Ecol. Evol 9, 460–464. 10.1111/2041-210X.12874.

103. Friard O, and Gamba M (2016). BORIS: a free, versatile open-source event-logging software for video/audio coding and live observations. Methods Ecol. Evol 7, 1325–1330. 10.1111/2041-210X.12584.

104. Clements JD, and Bekkers JM (1997). Detection of spontaneous synaptic events with an optimally scaled template. Biophys. J 73, 220–229. 10.1016/S0006-3495(97)78062-7. [PubMed: 9199786]

105. Rahmati V, Kirmse K, Marković D, Holthoff K, and Kiebel SJ (2016). Inferring Neuronal Dynamics from Calcium Imaging Data Using Biophysical Models and Bayesian Inference. PLOS Comput. Biol 12, e1004736. 10.1371/journal.pcbi.1004736. [PubMed: 26894748]

106. Fürth D, Vaissière T, Tzortzi O, Xuan Y, Märtin A, Lazaridis I, Spigolon G, Fisone G, Tomer R, Deisseroth K, et al. (2018). An interactive framework for whole-brain maps at cellular resolution. Nat. Neurosci 21, 139–149. 10.1038/s41593-017-0027-7. [PubMed: 29203898]

107. Minkowicz S, Mathews Mychaela A, Mou Felicia H, Yoon H, Freda SN, Ethan C, Kennedy A, and Kozorovitskiy Y (2023). Striatal ensemble activity in an innate naturalistic behavior. Elife 12. 10.7554/ELIFE.87042.

108. Freda SN, Priest MF, Badong D, Xiao L, Liu Y, and Kozorovitskiy Y (2022). Brainwide input-output architecture of paraventricular oxytocin and vasopressin neurons. bioRxiv, 2022.01.17.476652. 10.1101/2022.01.17.476652.

Highlights:

- Acute sleep deprivation induces dopamine-dependent affective state transitions
- Sleep loss enhances dopamine release in distributed brain regions
- Distinct dopaminergic pathways modulate specific behaviors during state transitions
- New dendritic spines in mPFC maintain reversal of depressive state after sleep loss

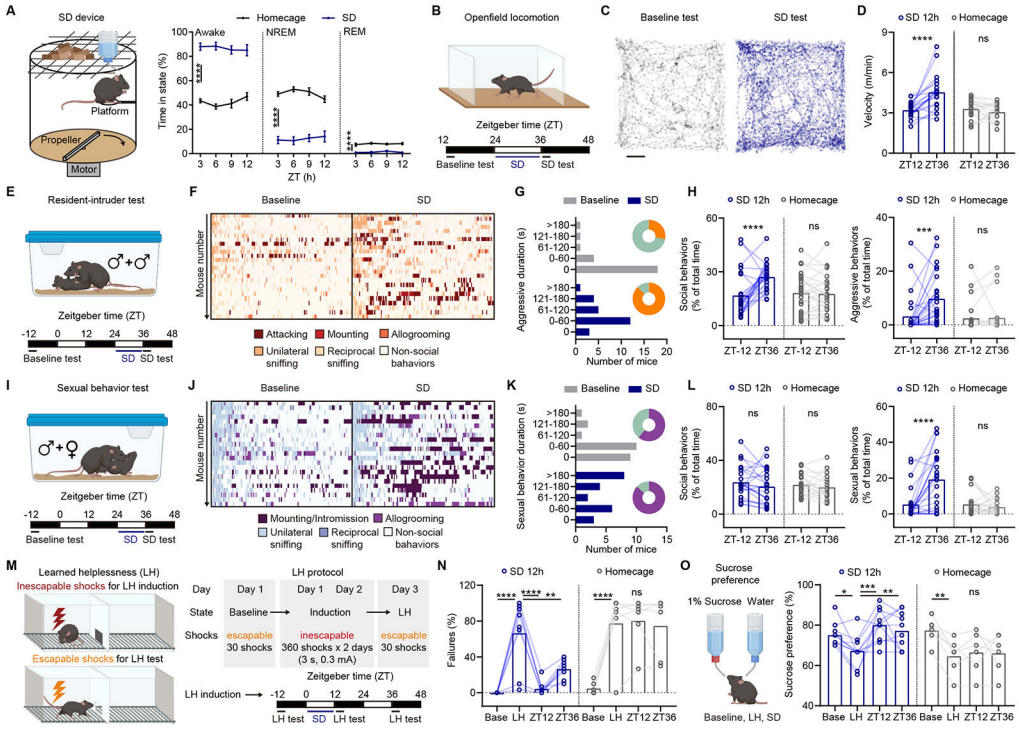

Figure 1. Acute sleep deprivation induces behavioral state transitions

(A). Left, schematic of the hybrid sleep deprivation (SD) apparatus. Right, validation by EEG and EMG recording. n = 4-5 animals/group. Two-way ANOVA, homecage vs SD, Awake, $p < 0.0001$, NREM, $p < 0.0001$, REM, $p < 0.0001$.

(B). Schematic showing the timeline for open field locomotion tests before (grey) and after (blue) SD.

(C). Trajectories of locomotor activity in the baseline and SD conditions for one mouse (10 min). Scale bar: 5 cm.

(D). Summary data showing the distance traveled in the open field locomotion test at ZT12 and ZT36 for SD and homecage control mice. n = 21 (SD) and 15 (homecage). Two-way ANOVA, interaction, $p = 0.0003$, Sidak's multiple comparison, ZT12 vs ZT36, SD, $p < 0.0001$, homecage, $p = 0.6714$.

(E). Schematic showing the timeline for resident-intruder tests before and after SD.

(F). Plots showing behavioral motif classifications in individual resident mice before and after SD.

(G). Distribution of aggressive behavior in mice before and after SD, based on time spent attacking smaller male conspecifics. Pie charts show the proportion of mice displaying aggressive behaviors (orange) before and after acute SD. n = 25.

(H). Left, summary data show the total time spent engaged in social interactions during the resident-intruder test at ZT-12 and ZT36. n = 25 (SD) and 25 (homecage). Two-way ANOVA, interaction, $p = 0.0011$, Sidak's multiple comparison, ZT-12 vs ZT36, SD, $p < 0.0001$, homecage, $p = 0.9649$. Right, same as left but for aggressive behaviors. Two-way ANOVA, interaction, $p = 0.0082$, Sidak's multiple comparison, ZT-12 vs ZT36, SD, $p = 0.0004$, homecage, $p = 0.9924$.

(I). Schematics showing the timeline for sexual behavior tests before and after SD.

(J). Plots show behavioral motif classifications of individual resident mice towards receptive females before and after SD.
(K). Distribution of sexual behavior timing in mice before and after SD, based on time spent engaging in sexual behaviors with a receptive female. Pie charts show the proportion of mice displaying sexual behaviors (purple) before and after acute SD. n = 23.
(L). Left, summary data show the total time spent interacting with receptive females for the male residents at ZT-12 and ZT36. n = 23 (SD) and 18 (homecage). Two-way ANOVA, interaction, $p = 0.6662$, Sidak's multiple comparison, ZT-12 vs ZT36, SD, $p = 0.2711$, homecage, $p = 0.7181$. Right, same as left, but for mounting behavior. Two-way ANOVA, interaction, $p = 0.0002$, Sidak's multiple comparison, ZT-12 vs ZT36, SD, $p < 0.0001$, homecage, $p = 0.8430$.
(M). Schematics show the timeline for learned helplessness (LH) induction and escape tests before and after SD.
(N). Summary data show the percentage of failures to escape an avoidable foot-shock across conditions. n = 8 (SD) and 6 (homecage). Two-way ANOVA, interaction, $p < 0.0001$. Sidak's multiple comparison test vs LH, Baseline, $p < 0.0001$ (SD), $p < 0.0001$ (homecage), ZT12, $p < 0.0001$ (SD), $p > 0.9999$ (homecage), ZT36, $p = 0.0018$ (SD), $p > 0.9999$ (homecage).
(O). Left, schematics show the conditions for sucrose preference test. Right, summary data show the percentage of sucrose preference by volume consumed across conditions. n = 10 (SD) and 6 (homecage). Two-way ANOVA, interaction, $p = 0.0017$. Holm-Sidak's multiple comparison test vs LH, Baseline, $p = 0.0345$ (SD), $p = 0.0053$ (homecage), ZT12, $p = 0.0002$ (SD), $p > 0.9307$ (homecage), ZT36, $p = 0.0053$ (SD), $p > 0.9307$ (homecage). Male mice were used in the tests for behavioral evaluation across multiple categories. *$p < 0.05$, ** $p < 0.01$, *** $p < 0.001$, **** $p < 0.0001$. ns, not significant. Error bars reflect SEM.
See also Figure S1-4.

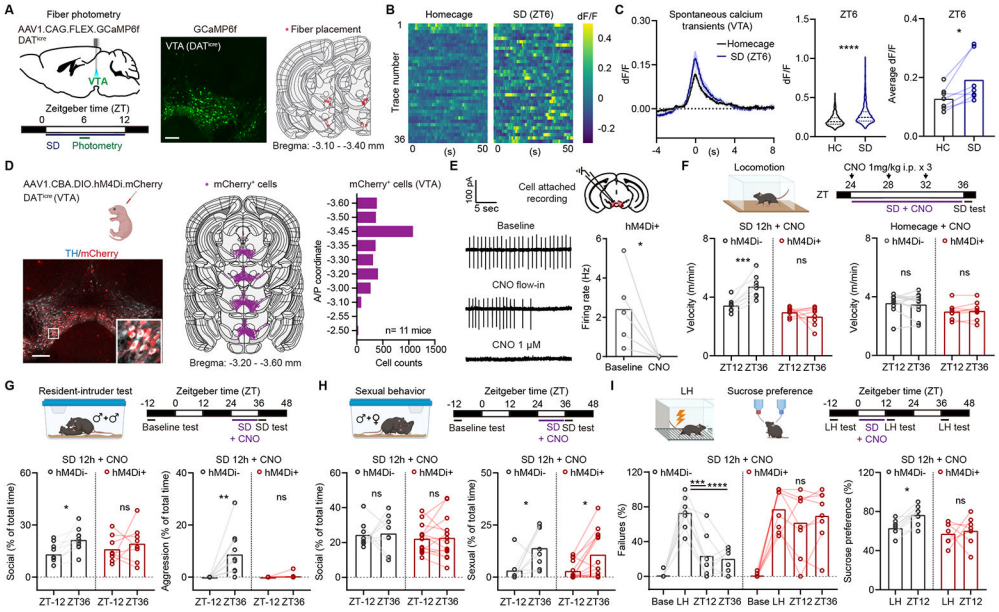

Figure 2. State transitions after sleep deprivation engage VTA DA neuron activity

(A). Left, schematic showing viral transduction and the timeline of photometry recording during SD. Middle, histological image showing the expression of GCaMP6f in the VTA. Scale bar: 200 μm. Right, fiber placement in coronal brain sections registered to the Common Coordinate Framework, 1–2 sections for each animal. n = 7 animals.

(B). Heatmap plots showing spontaneous VTA DA calcium transients at ZT6 in the home cage or during SD. Sequential traces from a single mouse are plotted.

(C). Left, average spontaneous calcium transients in VTA DA neurons in the home cage or during SD from all animals, with peak dF/F aligned to zero. Middle, violin plots show amplitude distribution of spontaneous calcium transients in the home cage (520 transients, 75.1 ± 8.5) and during SD (569 transients, 80.86 ± 4.1) from 7 animals, Two-tailed unpaired t test, $p < 0.0001$. Right, the average amplitude of spontaneous calcium transients for 7 individual animals in the home cage or during SD, Two-tailed paired t test, $p = 0.0221$.

(D). Left, schematic showing neonatal viral transduction and hM4Di-mCherry expression in tyrosine hydroxylase (TH) expressing cells in the VTA. Scale bar: 200 μm. Middle, mCherry expression in single neurons in coronal sections registered to the Common Coordinate Framework. Right, summary data showing the number of $mCherry^+$ cells across the anterior-posterior axis.

(E). Left, cell-attached recording of spontaneous spiking in mCherry+ VTA neuron before, during, and after bath application of 1 μM clozapine-N-oxide (CNO). Right, summary data showing the firing rate of $hM4Di^+$ neurons before and after CNO application. Two-tailed paired t test, $p = 0.0479$. n = 5 cells from 2 animals.

(F). Top, schematic showing the timeline of locomotion tests and CNO administration. Bottom left, summary data of distance traveled in the open field locomotion tests at ZT12 and ZT36 with CNO treatment for $hM4Di^-$ and $hM4Di^+$ mice. Two-way ANOVA, Sidak's multiple comparison, ZT12 vs ZT36, $hM4Di^-$, $p = 0.0003$, $hM4Di^+$, $p = 0.4304$. Bottom right, same as left, but for homecage controls, Two-way ANOVA, Sidak's multiple

comparison, ZT12 vs ZT36, hM4Di$^-$, p = 0.7479, hM4Di$^+$, p = 0.9621. n = 8 animals/group (SD). n = 11 hM4Di$^-$ and 8 hM4Di$^+$ (homecage).

(G). Top, schematic shows the timeline for resident-intruder tests before and after SD with CNO treatment. Bottom left, summary data for the total time spent in social interactions during the resident-intruder test for hM4Di$^-$ and hM4Di$^+$ mice at ZT-12 and ZT36. n = 10 hM4Di$^-$ and 8 hM4Di$^+$ animals. Two-way ANOVA, Sidak's multiple comparison, ZT-12 vs ZT36, hM4Di$^-$, p = 0.0375, hM4Di$^+$, p = 0.6194. Bottom right, same as left but for aggressive behaviors. Two-way ANOVA, Sidak's multiple comparison, ZT-12 vs ZT36, hM4Di$^-$, p = 0.0011, hM4Di$^+$, p = 0.9766.

(H). Top, schematic shows the timeline for sexual behavior tests before and after SD with CNO treatment. Bottom left, summary data for the total time spent in social interactions for hM4Di$^-$ and hM4Di$^+$ mice at ZT-12 and ZT36. n = 8 hM4Di$^-$ and 14 hM4Di$^+$. Two-way ANOVA, Sidak's multiple comparison, ZT-12 vs ZT36, hM4Di$^-$, p = 0.9778, hM4Di$^+$, p = 0.9809. Bottom right, same as left but for sexual behaviors. Two-way ANOVA, Sidak's multiple comparison, ZT-12 vs ZT36, hM4Di$^-$, p = 0.0194, hM4Di$^+$, p = 0.0242.

(I). Top, schematic shows the timeline of LH escape tests before and after SD with CNO treatment. Bottom left, summary data for the percentage of failures to escape across conditions in hM4Di$^-$ and hM4Di$^+$ mice. n = 7 hM4Di$^-$ and 8 hM4Di$^+$ animals. Two-way ANOVA, Sidak's multiple comparison test vs LH, ZT12, p = 0.0001 (hM4Di$^-$), p = 0.7238 (hM4Di$^+$), ZT36, p < 0.0001 (hM4Di$^-$), p = 0.9976 (hM4Di$^+$). Bottom right, same as left but for sucrose preference, n = 9 hM4Di$^-$ and hM4Di$^+$ animals. Two-way ANOVA, Holm-Sidak's multiple comparison test LH vs ZT12, p = 0.0437 (hM4Di$^-$), p = 0.6207 (hM4Di$^+$).

Male and female mice were tested in A-F, and I. Male mice were tested in G and H.

*p < 0.05, ** p < 0.01, *** p < 0.001, **** p < 0.0001. ns, not significant.

See also Figure S5.

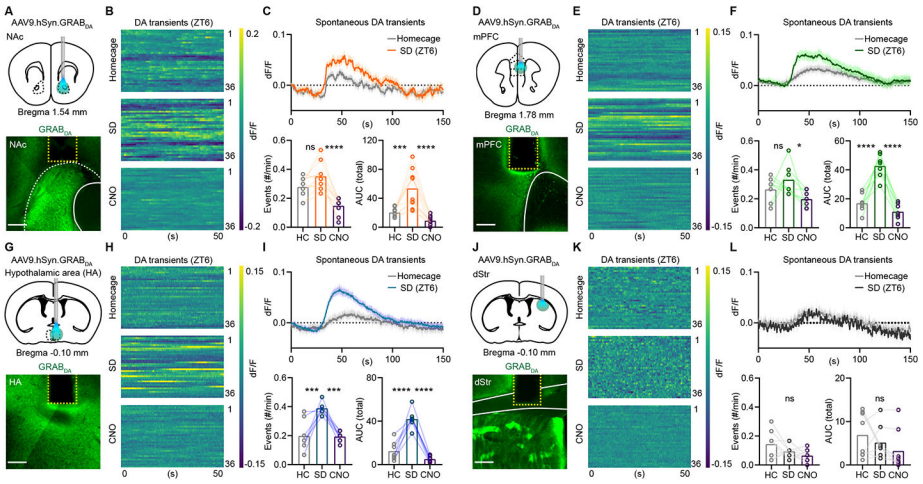

Figure 3. Sleep deprivation shapes spontaneous dopamine release

(A). Top, schematic showing viral transduction of AAV9.hSyn.GRAB$_{DA}$ in the Nucleus Accumbens (NAc). Bottom, image showing the expression of GRAB$_{DA}$ in the NAc and fiber placement. Scale bar: 200 μm.

(B). Heatmap plots showing spontaneous DA transients in the NAc at ZT6 in the home cage, during SD, and following chemogenetic inhibition of VTA DA neurons (CNO 1mg/kg, i.p.).

(C). Top, average trace of spontaneous DA transients in the NAc in the home cage (93 transients) and during SD (115 transients) from 10 animals. Transients were aligned to onset at t = 30 sec. Bottom left, summary data showing the frequency (events/min) of spontaneous DA transients from individual animals in the home cage, during SD, and following CNO administration (n = 10). RM One-way ANOVA, $p < 0.0001$. Sidak's multiple comparison test, HC vs SD, $p = 0.1027$, SD vs CNO, $p < 0.0001$. Bottom right, the cumulative area under the curve (AUC) for all spontaneous DA transients in 30-minute-long GRAB$_{DA}$ photometry recordings from individual animals. RM One-way ANOVA, $p < 0.0001$. Sidak's multiple comparison test, HC vs SD, $p = 0.0002$, SD vs CNO, $p < 0.0001$.

(D-E). Same as (A-B), but for DA transients in the mPFC.

(F). Top, average spontaneous DA transients in the mPFC in the home cage (62 transients) and during SD (76 transients) from 7 animals. Bottom left, RM One-way ANOVA, $p = 0.0318$. Sidak's multiple comparison test, HC vs SD, $p = 0.4168$, SD vs CNO, $p = 0.0285$. Bottom right, RM One-way ANOVA, $p < 0.0001$. Sidak's multiple comparison test, HC vs SD, $p < 0.0001$, SD vs CNO, $p < 0.0001$.

(G-H). Same as (A-B), but for DA transients in the hypothalamic area (HA).

(I). Top, average spontaneous DA transients in the HA in the home cage (49 transients) and during SD (88 transients) from 7 animals. Bottom left, RM One-way ANOVA, $p < 0.0001$. Sidak's multiple comparison test, HC vs SD, $p = 0.0003$, SD vs CNO, $p = 0.0002$. Bottom right, RM One-way ANOVA, $p < 0.0001$. Sidak's multiple comparison test, HC vs SD, $p < 0.0001$, SD vs CNO, $p < 0.0001$.

(J-K). Same as (A-B), but for DA transients in the dorsal striatum (dStr).

(L). Top, average spontaneous DA transients in the dStr in the home cage (35 transients) and during SD (23 transients) from 8 animals. Bottom left, RM One-way ANOVA, $p = 0.0673$. Sidak's multiple comparison test, HC vs SD, $p = 0.3556$, SD vs CNO, $p = 0.7575$. Bottom

right, RM One-way ANOVA, p = 0.2862. Sidak's multiple comparison test, HC vs SD, p = 0.8326, SD vs CNO, p = 0.7848.

Male and female mice were tested in A-L.

*p < 0.05, *** p < 0.001, **** p < 0.0001. ns, not significant.

See also Figure S6 and S7.

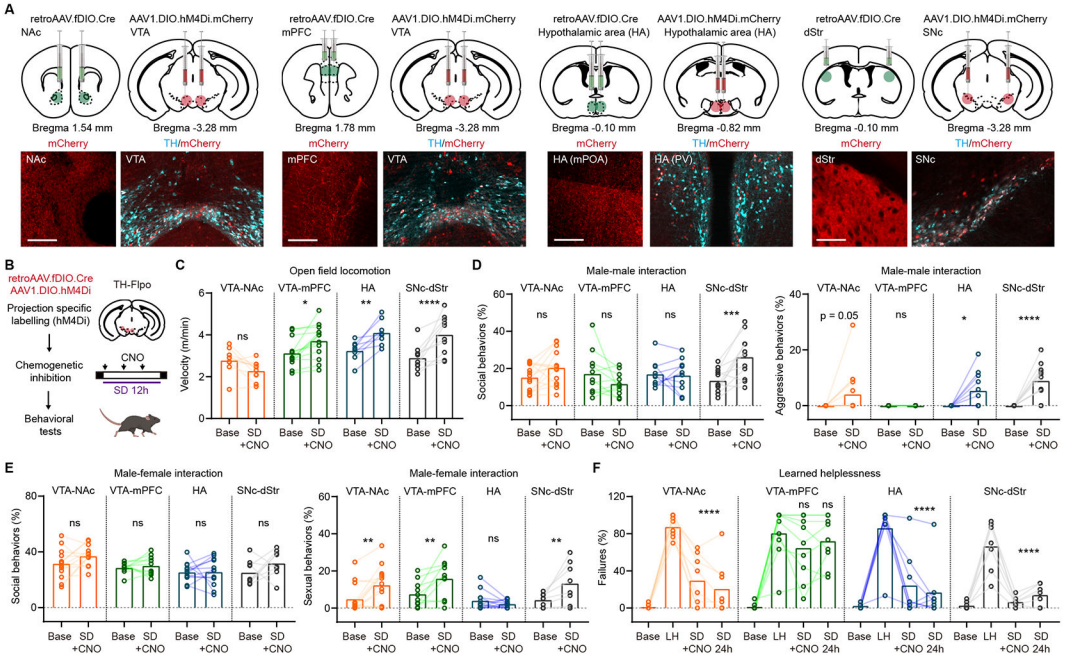

Figure 4. Distinct DA neuronal projections mediate SD-associated behavioral shifts

(A). Top, schematic shows projection-specific viral transduction strategies for targeting NAc-projecting, mPFC-projecting, locally projecting hypothalamic, and dStr-projecting DA neurons. Bottom, histological images show mCherry$^+$ DA axonal terminals, mCherry$^+$ cell bodies and TH$^+$ cell bodies in relevant brain regions. Scale bar: 200 μm.

(B). Schematic showing the timeline of CNO administration and behavioral tests.

(C). Summary data for distance traveled in the open field locomotion in baseline and after SD with chemogenetic inhibition of different subgroups of hM4Di$^+$ DA neurons. Two-way ANOVA, Sidak's multiple comparison, Baseline vs SD + CNO, VTA-NAc (n = 10), p = 0.0827, VTA-mPFC (n = 13), p = 0.0106, HA (n = 8), p = 0.0028, SNc-dStr (n = 10), p < 0.0001.

(D). Left, summary data for social interactions in resident-intruder tests in baseline and after SD with chemogenetic inhibition of different subgroups of hM4Di$^+$ DA neurons. Two-way ANOVA, Sidak's multiple comparison, Baseline vs SD + CNO, VTA-NAc (n = 15), p = 0.1995, VTA-mPFC (n = 11), p = 0.3045, HA (n = 10), p = 0.9993, SNc-dStr (n = 11), p = 0.0007. Right, same as left, but for aggressive behaviors. Two-way ANOVA, Sidak's multiple comparison, Baseline vs SD + CNO, VTA-NAc, p = 0.0490, VTA-mPFC, p > 0.9999, HA, p = 0.0219, SNc-dStr, p < 0.0001.

(E). Left, summary data for social interactions with receptive females in baseline and after SD with chemogenetic inhibition of different subgroups of hM4Di$^+$ DA neurons. Two-way ANOVA, Sidak's multiple comparison, Baseline vs SD + CNO, VTA-NAc (n = 13), p = 0.3292, VTA-mPFC (n = 10), p = 0.9897, HA (n = 12), p > 0.9999, SNc-dStr (n = 9), p = 0.3181. Right, same as left, but for sexual behaviors. Two-way ANOVA, Sidak's multiple comparison, Baseline vs SD + CNO, VTA-NAc, p = 0.0046, VTA-mPFC, p = 0.0058, HA, p = 0.8924, SNc-dStr, p = 0.0092.

(F). Summary data for the percentage of failures to escape across conditions in mice with chemogenetic inhibition of hM4Di$^+$ neurons during SD. Two-way ANOVA, Sidak's multiple

comparison test vs LH, VTA-NAc (n = 8), SD + CNO, SD 24h, $p < 0.0001$; VTA-mPFC (n = 9), SD + CNO, $p = 0.5992$, SD 24h, $p = 0.9925$; HA (n = 8), SD + CNO, SD 24h, $p < 0.0001$; SNc-dStr (n = 7), SD + CNO, SD 24h, $p < 0.0001$.

Male and female mice were tested in C and F. Male mice were tested in D and E.

*$p < 0.05$, ** $p < 0.01$, *** $p < 0.001$, **** $p < 0.0001$. ns, not significant.

See also Figure S8.

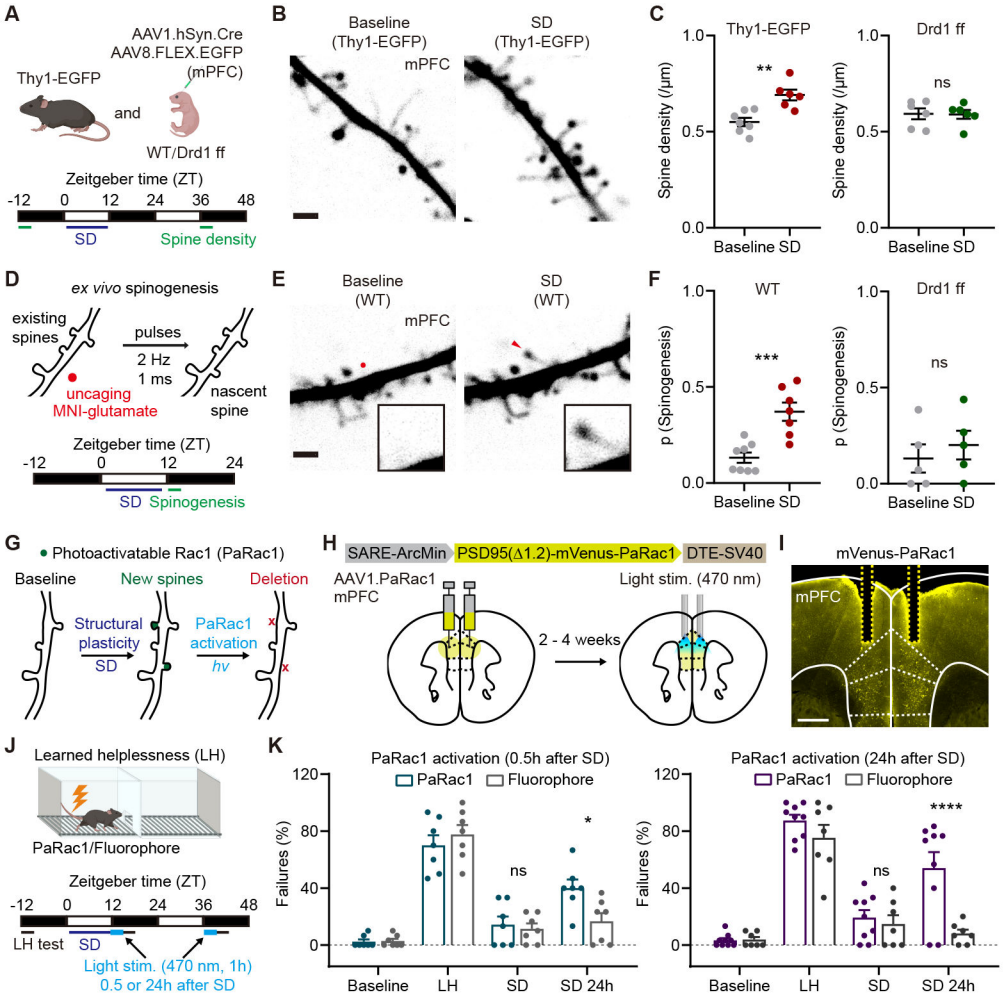

Figure 5. Antidepressant effects of acute sleep loss require Drd1-dependent enhancement of dendritic spine plasticity

(A). Top, schematic showing neonatal viral transduction of EGFP in wild type (WT) and Drd1^{ff} animals for dendritic spine density analysis and glutamate-evoked spinogenesis. Thy1-EGFP animals in WT background were only used for dendritic spine density analysis. Bottom, timeline of SD and dendritic spine density measurements.

(B). Example 2PLSM images of EGFP-expressing distal dendrites of deep layer mPFC pyramidal neurons in baseline condition and after SD, as noted. Scale, 2 μm.

(C). Summary data show dendritic spine density on distal dendrites from deep layer mPFC pyramidal neurons in WT (Thy1-EGFP, Left) and Drd1^{ff} (virally transduced EGFP, Right) animals in the baseline condition and after SD. Two-tailed unpaired t test, WT (n = 7 animals for baseline and 6 for SD), p = 0.0019, Drd1 ff (n = 6 animals/group), p = 0.9423.

(D). Top, schematic illustration of glutamate-evoked *de novo* spinogenesis platform with MNI-glutamate uncaging parameters for the induction of new dendritic spines. Bottom, timeline of SD and spinogenesis experiments.

(E). Example 2PLSM images of an example of successful induction of glutamate-evoked spinogenesis in an EGFP-expressing distal dendrite of deep layer mPFC pyramidal neuron. Scale bar, 2 μm.

(F). Summary data for the probability of spinogenesis on deep layer mPFC neurons in WT (Left) and Drd1^{ff} (Right) animals in baseline condition and after SD. Two-tailed unpaired t test, WT (n = 8 animals for baseline and 7 for SD), p = 0.0005, Drd1^{ff} (n = 5 animals/group), p = 0.5234.

(G). Schematic showing the shrinkage of newly formed dendritic spines induced by the photoactivation of PaRac1 after SD-induced plasticity changes.

(H). Schematic showing the design of PaRac1 construct and bilateral implantation of optical fibers following viral transduction.

(I). Image showing the expression of mVenus-PaRac1 and the location of fiber implantation. Scale bar: 500 μm.

(J). Schematics showing the timeline of LH test and PaRac1 activation after acute SD.

(K). Left, summary data for the percentage of failures to escape across conditions in mice with PaRac1 photoactivation 0.5h after SD. n = 7 animals/group. RM two-way ANOVA, Sidak's multiple comparison test, PaRac1 vs Fluorophore, Baseline, p > 0.9999, LH, p = 0.7653; SD, p = 0.9917, SD 24h, p = 0.0102. Right, same as left, but for photoactivation 24h after SD. n = 9 animals in PaRac1 and 7 in fluorophore. RM two-way ANOVA, Sidak's multiple comparison test, PaRac1 vs Fluorophore, Baseline, p > 0.9999, LH, p = 0.5539; SD, p = 0.9792, SD 24h, p < 0.0001.

Male and female mice were tested in A-K. *p < 0.05, **p < 0.01, *** p < 0.001, *** p < 0.001. ns, not significant. Dots represent data from individual animals. Error bars reflect SEM.

See also Figure S9.

KEY RESOURCES TABLE

REAGENT or RESOURCE	SOURCE	IDENTIFIER
Antibodies		
Rabbit anti-tyrosine hydroxylase	Millipore	Cat#AB152; RRID: AB_390204
Goat anti-RFP	Rockland	Cat# 200-101-379, RRID:AB_2744552
Rabbit anti-RFP	Rockland	Cat# 600-401-379, RRID:AB_2209751
Donkey anti-rabbit Alexa 647	Thermo Fisher Scientific	Cat# A-31573, RRID:AB_2536183
Donkey anti-goat Alexa 488	Thermo Fisher Scientific	Cat# A-11055, RRID:AB_2534102
Bacterial and Virus Strains		
AAV1.CAG.FLEX.GCaMP6f.WPRE-SV40	Chen TW., et al., 2013 Dr. Douglas Kim	Addgene viral prep; # 100835-AAV1
AAV9.hSyn.GRAB.DA2m	Sun et al., 2018 Dr. Yulong Li	Addgene viral prep #140553-AAV9
AAV1.CBA.DIO.hM4Di.mCherry	Hou XH., et al., 2016 Dr. Sabatini Packaged by Vigene	Addgene plasmid # 81008
retroAAV.EF1a.fDIO.Cre	Schneeberger et al., 2019 Esteban Engel & Alexander Nectow	Addgene viral prep #121675-AAVrg
AAV8.CAG.FLEX.EGFP	UNC Vector Core (Dr. Boyden)	N/A
AAV1.hSyn.Cre.WPRE.hGH	Penn vector core (Dr. Wilson)	Addgene viral prep # 105553-AAV1 Penn ID: AV-1-PV2676
Chemicals, Peptides, and Recombinant Proteins		
Clozapine-N-oxide	Sigma-Aldrich	C0823; CAS: 34233-69-7
MNI-caged-L-glutamate	Tocris	1490; CAS: 295325-62-1
β-Estradiol 3-benzoate	Sigma-Aldrich	E8515; CAS: 50-50-0
Progesterone	Sigma-Aldrich	P8783; CAS: 57-83-0
Polyethylenimine, Linear, MW 25000, Transfection Grade (PEI 25K™)	Polysciences	23966-1, CAS: 9002-98-6, 26913-06-4
Forskolin	Tocris	1099, CAS: 66575-29-9
Rac1 Activation Magnetic Beads Pulldown Assay	Millipore-Sigma	17-10393
Experimental Models: Organisms/Strains		
C57BL/6 mice	Charles River	Cat#000664; RRID: IMSR_JAX:000664
B6.SJL-*Slc6a3*$^{tm1.1(cre)Bkmn}$/J mice	Jackson Laboratory	Cat#006660; RRID: IMSR_JAX:006660
C57BL/6-Tg(Thy1-EGFP/SQSTM1)02Mcwo/J mice	Jackson Laboratory	Cat#027258; RRID:IMSR_JAX:027258
Th-2A-Flpo mice	Dr. Rajeshwar Awatramani	N/A
STOCK Drd1$^{tm2.1stl}$/J mice	Jackson Laboratory	Cat#025700; RRID: IMSR_JAX:025700
Recombinant DNA		
pTriEx-mVenus-PA-Rac1	Dr. Klaus Hahn, (Wu et al., 2009)	Addgene# 22007
pUCmini-iCAP-PHP.eB	Dr. Viviana Gradinaru	Addgene# 103005
pCAG-FLEX-mScarlet-WPRE	Dr. Ryan Larsen	Addgene # 99280
pHelper Vector	Cell Biolabs, Inc.	Cat. No. 340202
Software and Algorithms		

REAGENT or RESOURCE	SOURCE	IDENTIFIER
GraphPad Prism	GraphPad	RRID: SCR_002798
FIJI	Schindelin et al., 2012	http://fiji.sc/; RRID: SCR_002285
MATLAB	MathWorks	RRID: SCR_001622
Toxtrac	Rodriguez, A., et al., 2018	N/A
Python	Python Software Foundation	RRID:SCR_008394
pClamp	Molecular Devices	RRID:SCR_011323
Sleep Learning (SPINDLE)	Miladinović et al., 2019	N/A
Behavioral Observation Research Interactive Software (BORIS)	Friard and Gamba, 2016	RRID:SCR_021509
R Project for Statistical Computing	R Foundation R core team	RRID:SCR_001905
WholeBrain	Fürth et al., 2018	RRID:SCR_015245
Allen Mouse Brain Common Coordinate Framework	Allen Institute Wang et al., 2020	RRID:SCR_020999
Dendritic spine counter plugin	M. Voloshin, Mighty Data, Inc.	N/A
Other		
Active/Passive Avoidance Shuttle Box	MazeEngineers	https://mazeengineers.com/portfolio/active-passive-avoidance-shuttle-box/#description
Raspberry Pi	Raspberry Pi Foundation	https://www.raspberrypi.org/
Canadian Neurophotonics Platform Viral Vector Core Facility	N/A	RRID:SCR_016477